Core cross-linked polymeric micelles based on polypept(o)ides: from secondary structure formation of polypeptides to functional cross-linking strategies for polymeric micelles

Bauer, T.A.

6

Photocleavable Core Cross-Linked Polymeric Micelles of Polypept(o)ides and Ruthenium(II) Complexes

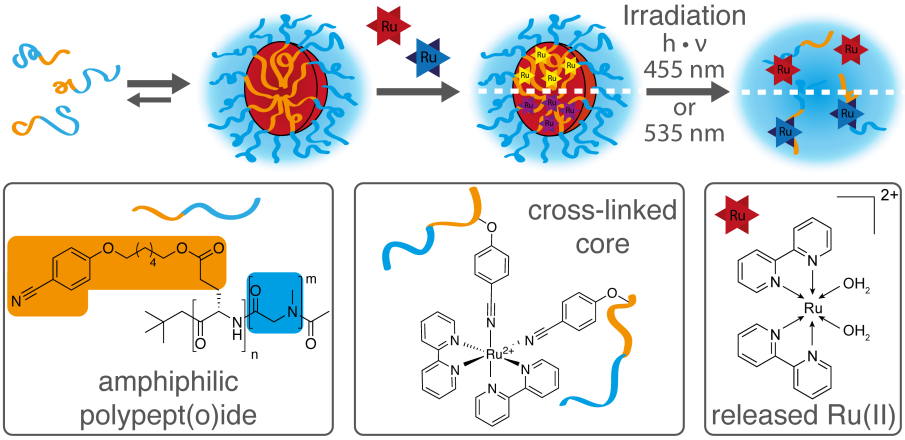

Published in Journal of Materials Chemistry B **2021**, *9*, 8211-8223.

DOI: 10.1039/D1TB01336J

Photocleavable Core Cross-Linked Polymeric Micelles of Polypept(o)ides and Ruthenium(II) Complexes

Tobias Alexander Bauer,[a,b] Jonas Eckrich,[c,d] Nadine Wiesmann,[c] Felix Kuczelinis,[b] Wen Sun,[e] Xiaolong Zeng,[e] Benjamin Weber,[b] Si Wu,[e] Nicolas Hubert Bings,[b] Sebastian Strieth,[c,d] Matthias Barz *[a,b]

Leiden Academic Centre for Drug Research (LACDR), Leiden University, Einsteinweg 55, 2333CC Leiden, The Netherlands.

Department of Chemistry, Johannes Gutenberg University Mainz, Duesbergweg 10-14, 55128 Mainz, Germany.

Department of Otorhinolaryngology, Head and Neck Surgery, University Medical Center Mainz, Langenbeckstr. 1, 55131 Mainz, Germany.

Department of Otorhinolaryngology, University Medical Center Bonn (UKB), Venusberg-Campus 1, 53127 Bonn, Germany.

Max Planck Institute for Polymer Research, Ackermannweg 10, 55128 Mainz, Germany.

Published in Journal of Materials Chemistry B **2021**, *9*, 8211-8223.

DOI: 10.1039/D1TB01336J

Abstract

Core cross-linking of polymeric micelles has been demonstrated to contribute to enhanced stability that can improve the therapeutic efficacy. Photochemistry has the potential to provide spatial resolution and on-demand drug release. In this study, light-sensitive polypyridyl-ruthenium(II) complexes were combined with polypept(o)ides for photocleavable core cross-linked polymeric micelles. Block copolymers of polysarcosine-*block*-poly(glutamic acid) were synthesized by ring-opening *N*-carboxyanydride polymerization and modified with aromatic nitrile-groups on the glutamic acid side chain. The modified copolymers self-assembled into micelles and were cross-linked by *cis*-diaquabis(2,2'-bipyridine)-ruthenium(II) ($[Ru(bpy)_2(H_2O)_2]^{2+}$) or *cis*-diaquabis(2,2'-bisquinoline)-ruthenium(II) ($[Ru(biq)_2(H_2O)_2]^{2+}$). Depending on the flexibility of the nitrile linker, either small spherical structures (D_h 45 nm, PDI 0.11) or worm-like micelles were obtained. The cross-linking reaction did not affect the overall size distribution but induced a change in the metal-to-ligand charge transfer peak from 482 to 420 nm and 592 to 548 nm. The cross-linked micelles displayed colloidal stability after incubation with human blood plasma and during gel permeation chromatography in hexafluoroisopropanol. Light-induced cleavage of $[Ru(bpy)_2(H_2O)_2]^{2+}$ was accomplished within 300s, while $[Ru(biq)_2(H_2O)_2]^{2+}$ could not be completely released. Analysis in HuH-7 cells revealed increased cytotoxicity via micellar delivery of $[Ru(bpy)_2(H_2O)_2]^{2+}$ but mostly irradiation damage for $[Ru(biq)_2(H_2O)_2]^{2+}$. Further evaluation *in ovo* confirmed stable circulation pointing towards the future development of quick-release complexes.

Cover page

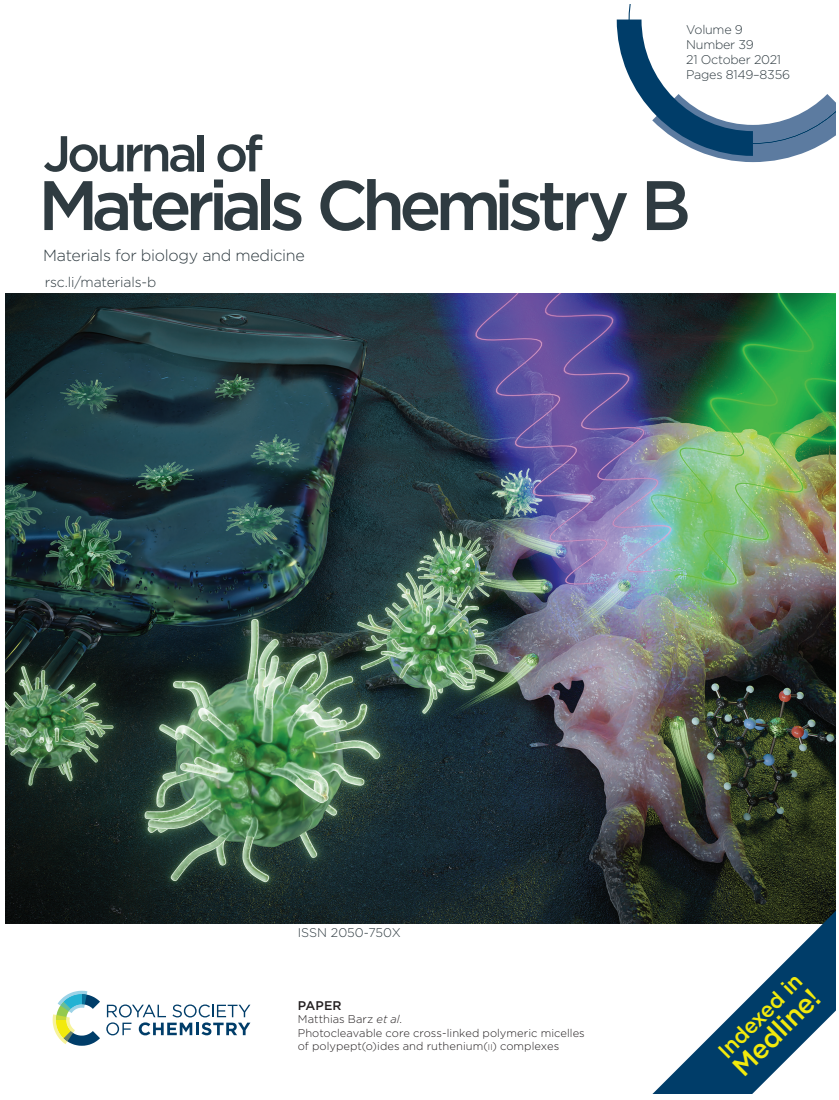

Polypept(o)ides and ruthenium(II) complexes feature photocleavable core cross-linked polymeric micelles with tuneable size and morphology. Irradiation induces ligand exchange and release of pro-drug ruthenium(II) complexes for photoactivated chemotherapy. The functional design provides spatial resolution to therapeutic intervention.

Introduction

Polymeric micelles have emerged to solubilize hydrophobic drugs and could already demonstrate to improve the off-target toxicity and biodistribution of pharmaceutical agents for applications ranging from cancer treatment to inflammatory diseases.[1–4] To prevent rapid carrier disintegration and premature drug release after intravenous administration, additional stabilization strategies are required. This calls for the next generation of polymeric micelles and for specific delivery beyond replacing low molecular weight surfactants in drug formulations.[5–8] Stabilization by non-covalent interaction, e.g., by π-π-stacking seems promising and simple yet is barely understood in its full depth for drug delivery systems with triggered release profiles.[9–13] Cross-linking by dynamic covalent bonds is thus a straightforward approach accounting for drug release by either disease-related or external stimuli.[5] Free radical cross-linking of thermosensitive poly(ethylene glycol)-*b*-poly(*N*-(2-hydroxypropyl) methacrylamide)-based copolymers has been combined with a pH-sensitive docetaxel-pro drug cross-linker (CPC634) and is currently under clinical investigation in phase II studies for the treatment of ovarian cancer.[14,15] In clinical phase I studies, the delivery of docetaxel by CPC634 increased the total intratumoral drug concentration by 4-fold compared to Taxol.[16] Nevertheless, a close-up study revealed that the majority of docetaxel was still conjugated to the carrier, which underscores the importance of carrier stability but comprehensive and controlled drug release.[16,17] To reduce the dose-limiting nephrotoxicity of free cisplatin, Kataoka and co-workers introduced NC-6004, in which the platin(II) complex is covalently conjugated to block copolymers of poly(ethylene glycol)-*block*-poly(glutamic acid) (pGlu).[18,19] The exchange of cisplatin's chloride ligands by the carboxylate group of the pGlu side chain induces self-assembly into small spherical core cross-linked polymeric micelles ($D_h \approx 30$ nm). Under physiological conditions, cisplatin is released from the carrier by an erosion process leading to an 11-fold higher area under the curve for NC-6004 compared to conventional cisplatin.[20] The given examples demonstrate how the pharmacologic profile of a drug can be altered by nanomedicine. In combination with photoactivated chemotherapy, actual spatial control over drug release can be added, as cytotoxic agents are activated only at the location of interest by irradiation.[21,22] In reminiscence of cisplatin, ruthenium(II) complexes were found to bind to DNA leading to cytotoxicity but also exhibit rich photochemistry.[23–27] In particular, polypyridyl-ruthenium(II) complexes have been thoroughly investigated and

could be successfully integrated into amphiphilic metallopolymers that self-assembled to polymeric micelles.[28–30] Upon irradiation at the metal-to-ligand charge transfer (MLCT) peak, the ruthenium pro-drugs were cleaved from the polymer backbone, which inhibited tumor growth *in vitro* and *in vivo* by uncaging cytotoxic agents and additional production of singlet oxygen.[28–31]

We now propose to expand these features to core cross-linked polymeric micelles by combining ruthenium(II) complexes with polypept(o)ides. Polypept(o)ides comprise a novel material class of hybrid copolymers that connect the shielding properties of polysarcosine (pSar) with the functional diversity of polypeptides.[32–34] The polymeric architectures thereof can be easily synthesized by living ring-opening *N*-carboxyanhydride (NCA) polymerization.[32,35–37] For nanomedicine applications, pSar, poly(*N*-methyl glycine), provides water solubility and prevents unspecific interaction with proteins, whereas polypeptides allow for stimuli-responsiveness and drug conjugation at the functional amino acid side chain.[38–43] Due to its low immunogenic profile and the potential to evade the accelerated blood clearance phenomenon, pSar is considered a promising substitute for poly(ethylene glycol) but is based on an endogenous amino acid.[39,44–46]

Experimental

Materials and Methods. Unless stated otherwise, solvents were purchased from Sigma Aldrich and used as received. Tetrahydrofuran (THF) was dried over Na and freshly distilled prior to use. *N*,*N*-Dimethyl formamide (DMF) was bought from Acros (99.8%, extra dry over molecular sieve) and purified by repetitive freeze-thaw cycles to remove dimethylamine prior to use. Dry dimethyl sulfoxide (DMSO) (99.7%, extra dry, over molecular sieve) was obtained from Acros and used without further purification. MilliQ water was prepared using a MILLI-Q® Reference A+ System. Water was used at a resistivity of 18.2MΩ·cm and total organic carbon of <5 ppm. Hexafluoroisopropanol (HFIP) was purchased from Fluorochem. Deuterated solvents were obtained from Deutero GmbH and were used as received. Nanoparticle purification was performed by Amicon Ultra spin filters (MWCO 3 kDa, 10 kDa or 100 kDa) with ethanol/water mixtures or MilliQ water. Centrifugation was carried out in a Thermo Scientific Heraeus Multifuge 1 or in a Thermo Scientific Heraeus MFresco centrifuge. Photos were recorded with a Nikon D90 digital single lens reflex camera.

NMR Spectroscopy. ^{1}H NMR spectra were recorded on a Bruker Avance II 400 (400 MHz) at room temperature at a frequency of 400 MHz. Diffusion ordered

spectroscopy (DOSY) data were recorded on a Bruker Avance III HD 400 (400 MHz). Calibration of the spectra was achieved using the solvent signals. NMR spectra were analyzed with MestReNova version 12.0.4 from Mestrelab Research S.L. Degrees of polymerization (X_n) by ^{1}H NMR were calculated comparing the integral of the initiator peak and the integrals of the α-protons for pSar and pGlu(O*t*Bu), respectively.

Infrared Spectroscopy. Attenuated total reflectance Fourier transform infrared (ATR-FT-IR) spectroscopy was performed on a FT/IR-4100 (JASCO Corporation) with an ATR sampling accessory (MIRacle, Pike Technologies). IR spectra were analyzed using Spectra Manager 2.0 (JASCO Corporation). NCA polymerization was judged to be completed when NCA-associated carbonyl peaks at 1853 and 1786 cm^{-1} had vanished.

Gel Permeation Chromatography. Analytical gel permeation chromatography (GPC) was performed at 40 °C using HFIP as the eluent, which was equipped with 3 g·L^{-1} potassium trifluoroacetate. The column material was modified silica gel (PFG columns, particle size: 7 µm, porosity: 100 Å and 4000 Å), purchased from PSS Polymer Standards Service GmbH. For polymer detection a UV detector (JASCO UV-2075+) at a wavelength of λ = 230 nm (or λ = 565 nm, as indicated) was employed. Molecular weights were determined by using a calibration with poly(methyl methacrylate) (PMMA) (PSS Polymer Standards Services GmbH) and pSar standards with toluene as internal standard. The elution diagram was evaluated with PSS WinGPC (PSS Polymer Standard Service GmbH).

Single-Angle DLS and Zeta Potential. Single-angle dynamic light scattering (DLS) experiments and ξ-potential measurements were performed with a ZetaSizer Nano ZS instrument (Malvern Instruments Ltd., Worcestershire, UK) equipped with a He-Ne laser (λ = 632.8 nm) as the incident beam. All DLS measurements were performed at 25 °C and a detection angle of 173°. Zeta potential was determined in MilliQ water equipped with 3 mm sodium chloride. For aggregation experiments, polymers were dissolved in DMSO (5 g·L^{-1}), water was added, and the count rate was measured at equal time intervals.

UV-Vis Spectroscopy. UV-Vis spectra were recorded using a Jasco V-630 spectrophotometer (1 cm × 1 cm quartz cell). Visible light irradiation was performed with high brightness light emitting diodes (LEDs) and UV-Vis measurements were performed at the indicated time points.

Multi-Angle DLS. For multi-angle DLS, cylindrical quartz cuvettes (Hellma, Mühlheim, Germany) were cleaned by dust-free distilled acetone and transferred to a dust free flow box. Solutions were filtered into the cuvettes through Pall GHP filters, 0.45 µm pore size. DLS measurements were performed by the following instrument at 20 °C. The apparatus consists of a Uniphase He/Ne Laser (22.5 mW output power at λ = 632.8 nm) and an ALV/CGS-8F SLS/DLS 5022F goniometer with eight simultaneously working ALV 7004 correlators and eight ALV/High QEAPD avalanche photodiode detectors. The correlation functions of the particles were fitted using a sum of two exponentials. The z-average diffusion coefficient Dz was calculated by extrapolating D_{app} for q = 0. By formal application of Stokes law, the inverse z-average hydrodynamic radius is $R_h = \langle R_h^{-1} \rangle_z^{-1}$. To investigate the aggregation behavior of the particles in human plasma,[47] citrate plasma pooled from 6 probands was used. Plasma was obtained from the university medical center Mainz and filtered through a Millex GS 0.22 µm filter. The particle solutions were filtered through 0.45 µm pore size Pall GHP filters. The following mixtures have been prepared: plasma/PBS 9:1 and plasma/particle solution 9:1 (β = 0.01 g·L^{-1}). The cuvettes were incubated for 20 min at room temperature before measurement.

Atomic Force Microscopy. Atomic force microscopy (AFM) was measured on mica using a CypherTM AFM (Asylum Research) using tapping mode at a scan rate of 1 Hz. Samples were prepared by drop-casting of a particle solution (β = 50 mg·L^{-1} in MilliQ water) onto freshly cleaned mica. The sample was dried overnight at room temperature. Images were evaluated and apparent height profiles were extracted using Gwyddion 2.49.

Transmission Electron Microscopy. Transmission electron microscopy (TEM) was performed on a FEI Tecnai G2 Spirit microscope equipped with a Gatan US1000 2k x 2k CCD camera and LaB_6 cathode operated at 120 kV. Images were recorded using freshly glow discharged carbon coated copper grids (CF300-Cu, 300 mesh). For non-stained samples, 5 µL nanoparticle solution (β = 50 mg·L^{-1} in MilliQ water) was drop-coated on the TEM grid surface and removed with a filter paper after 1 min. For negatively stained samples, 5 µL nanoparticle solution (β = 50 mg·L^{-1} in MilliQ water) was drop-coated on the TEM grid, removed with a filter paper after 1 minute. Next, 5 µL uranyl acetate solution (2 wt.% in ethanol) were added and removed after 15 s incubation time. All sample-deposited grids were air-dried overnight before measurement. Software ImageJ 1.52h (National Institutes of Health, USA) was used for image evaluation.

Cryogenic Transmission Electron Microscopy. 5 µL of the nanoparticle solution (50 mg·L^{-1}, in MilliQ water) were applied to freshly glow-discharged carbon grids with a copper 200 mesh (Quantifoil Micro Tools GmbH). Excess fluid was removed by direct blotting (2.5 s) and the grids were individually plunge-frozen in liquid ethane. Grids were cryo-transferred in liquid nitrogen using a Gatan cryoholder (model 626 DH) to a Tecnai T12 transmission electron microscope equipped with a field emission electron source and operating at 120 kV accelerating voltage. Images were recorded using a TemCam-F416 (TVIPS, Gauting, Germany). Software ImageJ 1.52h (National Institutes of Health, USA) was used for image evaluation.

Solution Nebulization-Inductively Coupled Plasma-Mass Spectrometry. The Ru-concentration in the nanoparticles was determined using solution nebulization inductively coupled plasma-mass spectrometry (SN-ICP-MS). Therefore, 100 µL of each nanoparticle solution was diluted to 100 mL with ultrapure water (Millipore, Milli-Q System, USA). For quantification *via* external calibration solutions containing Ru at concentrations of 1, 3, 5, 7, 10, 20, 30, 40, 50, and 60 µg·L^{-1} were used. All solutions were acidified with HNO_3 (65% p.a. grade, Fluka, Honeywell, USA) to 2% (v/v) and 25 µg·L^{-1} of Rh were added as internal standard prior to ICP-MS analysis. For ICP-MS measurements a sample introduction system consisting of a concentric MicroMist™ nebulizer and a double pass spray chamber (Agilent Technologies, Santa Clara, CA, USA) were coupled to a quadrupole ICP-MS instrument 7800 (Agilent Technologies, Santa Clara, CA, USA). The signal intensities of $^{101}Ru^+$, $^{99}Ru^+$, and $^{103}Rh^+$ were measured for data evaluation. The optimum instrumental parameters of the developed ICP-MS method are as follows: plasma power: 1550 W, plasma gas flow rate: 15 L·min^{-1}, auxiliary gas flow rate: 0.9 L·min^{-1}, nebulizer gas flow rate: 0.99–1.05 L·min^{-1}, sampler and skimmer cone: Ni, data acquisition: 0.1 s integration time, 40 sweeps per replicate, 6 replicates.

Synthesis of Ruthenium (II) Complexes

***cis*-Diaquabis(2,2′-bipyridine)-ruthenium (II) bis(hexafluorophosphate) ([Ru(bpy)$_2$(H$_2$O)$_2$] (PF$_6$)$_2$).** The synthesis of $[Ru(bpy)_2(H_2O)_2](PF_6)_2$ was adapted and modified from Theis *et al.*[48] $Ru(bpy)_2Cl_2$ (300 mg, 0.620 mmol) was suspended in 15 mL water. The suspension was stirred at 80 °C under N_2 and after dissolution. The reaction mixture was heated for 4 h. After cooling to room temperature, the compound was precipitated with a saturated aqueous solution

of KPF_6. The orange powder was washed with a small amount of water and dried overnight. ^1H NMR (250 MHz, CD_2Cl_2) δ [ppm] = 10.19 (d, J = 5.7 Hz, 2H), 8.21 (d, J = 8.1 Hz, 2H), 8.06 (d, J = 8.1 Hz, 2H), 7.96 (m, J = 7.6 Hz, 2H), 7.64 (m, 4H), 7.54 (t, J = 7.8 Hz, 2H), 6.94 (t, J = 6.7 Hz, 2H).

cis-Diaquabis(2,2′-biquinoline)-ruthenium (II) bis(hexafluorophosphate) ([Ru(biq)$_2$(H$_2$O)$_2$] (PF$_6$)$_2$). The synthesis of $[Ru(biq)_2(H_2O)_2]$ $(PF_6)_2$ was adapted and modified from Sun *et al.*[29] $RuCl_3 \cdot H_2O$ (0.18 g, 0.67 mmol), 2,2′-biquinoline (0.37 g, 1.5 mmol), and LiCl (0.087 g, 2.1 mmol) were dissolved in 7 mL of DMF. The solution was stirred until all solids dissolved, was degassed with N_2 for 5 min, and was then refluxed for 24 h turning a dark green color. The reaction mixture was slowly cooled to room temperature and pipetted dropwise into 500 mL of stirring H_2O, forming a green precipitate that was collected by vacuum filtration. The solid was dissolved in CH_2Cl_2 forming a dark green solution, and then filtered to get rid of any remaining solid that did not dissolve. The green filtrate was washed 5 times with 20 mL of H_2O and then evaporated to a minimal amount of CH_2Cl_2. An excess of diethyl ether was added to the green CH_2Cl_2 solution, resulting in the formation of a green precipitate that was collected by vacuum filtration. The green solid ($Ru(biq)_2Cl_2$) was used for next step without any further purification (0.22 g, 48% yield). $Ru(biq)_2Cl_2$ (100 mg, 0.14 mmol) and $AgPF_6$ (46 mg, 0.29 mmol) were dissolved in 1:1 ethanol/H_2O mixture (10 mL). The solution was degassed and heated under reflux overnight in an argon atmosphere. The solution was cooled and filtered to remove AgCl. The solvent of the reaction was reduced to ~5 mL. Then, an aqueous solution of KPF_6 was added. The precipitate was filtered, washed with H_2O, and dried to obtain a blue solid ($[Ru(biq)_2(H_2O)_2](PF_6)_2$). ^1H NMR (250 MHz, acetone-d_6) δ [ppm] = 9.58 (d, J = 9.0 Hz, 1H), 8.88 (d, J = 8.8 Hz, 3H), 8.50 (m, 2H), 8.38 (m, 5H), 8.15 (m, 4H), 8.04 (d, J = 8.3 Hz, 2H), 7.59 (m, 3H), 6.97 (m, 4H).

Polymer Synthesis & Modification

All NCA monomers were prepared according to the Fuchs-Farthing method with purification by recrystallization (Glu(O*t*Bu)-NCA) or sublimation (Sar-NCA), as reported previously.[34,49]

Synthesis of poly(γ-tert-butyl-L-glutamic acid) (pGlu(OtBu)) and poly(γ-tert-butyl-L-glutamic acid)-block-poly(sarcosine) (pGlu(OtBu)-b-pSar) Neopentylamine (NPA)-initiated poly(γ-*tert*-butyl-L-glutamic acid)-*block*-poly(sarcosine) (pGlu(O*t*Bu)-*b*-pSar) was prepared *via* sequential NCA polymerization, as reported previously.[50]

Briefly, 394.5 mg (1.72 mmol; 30 eq.) of γ-*tert*-butyl-L-glutamic acid (Glu(O*t*Bu)) NCA were weighed into a pre-died Schlenk-flask, dissolved in anhydrous DMF (freshly amine-purified by freeze-thaw cycles) at a concentration of 200 g·L^{-1}, cooled to 0 °C, and NPA (5.0 mg; 57.4 µmol; 1.0 eq.) was added as a stock solution in THF (β_{NPA} = 10 g·L^{-1}). An amount of THF was added to ensure polymerization in a THF/DMF (1:1) mixture. After completed Glu(O*t*Bu)-NCA consumption, as monitored by FT-IR spectroscopy, a sample (P1) was taken for GPC-measurements and a solution of Sar-NCA (1.1 g; 9.18 mmol; 160 eq.) in dry DMF (β = 200 g·L^{-1}) was added and the polymerization was continued at 10 °C. For end-group-modification, acetic anhydride (54 µL; 0.57 mmol; 10 eq.) and *N*,*N*-diisopropylethylamine (DIPEA) (195 µL; 1.11 mmol; 20 eq.) were added and the solution was stirred for 1 day at room temperature. The obtained block copolymer was purified by repetitive (3x) precipitation and centrifugation (4500 rpm, 15 min, 4 °C) into a mixture of n-hexane and diethyl ether (2:1). The product (NPA-pGlu(O*t*Bu)$_{36}$-*b*-pSar$_{171}$-Ac) was dried in vacuo and obtained as a white powder (846 mg, 86%). ^{1}H NMR. pGlu(O*t*Bu)$_{36}$-*b*-pSar$_{171}$ (P2) (400 MHz, CD_2Cl_2), δ [ppm] = 8.45–8.13 (b s, 23H (1n), CON*H*), 4.40–3.78 (m, 366H (1n + 2m), α-C*H*$_{(pGlu)}$, α-C*H*$_{2(pSar)}$), 3.14–2.80 (m, 513H (3m), -C*H*$_{3(pSar)}$), 2.66–1.95 (m, 149H, β-C*H*$_{2(pGlu)}$, γ-C*H*$_{2(pGlu)}$), 1.53–1.35 (s, 324H (9n), -C*H*$_{3(pGlu)}$), 0.94–0.81 (b s, 9H, -C*H*$_{3(NPA)}$). HFIP-GPC, relative to PMMA standards. pGlu(O*t*Bu)$_{36}$ (P1): M_n = 19.7 kg/mol, M_w = 22.9 kg/mol; $Đ$ = 1.16. pGlu(O*t*Bu)$_{36}$-*b*-pSar$_{171}$ (P2): M_n = 44.0 kg/mol, M_w = 52.9 kg/mol; $Đ$ = 1.20.

Synthesis of poly(L-glutamic acid)-block-poly(sarcosine) (pGlu(OH)-b-pSar) PGlu(O*t*Bu)$_{36}$-*b*-pSar$_{171}$ (P2) was dissolved in a mixture of (45:45:5:5) DCM/trifluoroacetic acid (TFA)/triisopropylsilane (TIPS)/water and stirred for 3 h at 0 °C. Polymers were precipitated in ether, centrifuged (4000 rpm, 10 min, 4 °C) and the precipitate was dialyzed against aqueous $NaHCO_3$ solution and MilliQ water (MWCO 3.5 kDa), followed by lyophilization (yield 80%). ^{1}H NMR. pGlu(OH)$_{36}$-*b*-pSar$_{171}$ (P3) (400 MHz, D_2O), δ [ppm] = 4.55–4.02 (m, 373H (1n + 2m), α-C*H*$_{(pGlu)}$, α-C*H*$_{2(pSar)}$), 3.13–2.77 (m, 513H (3m), -C*H*$_{3(pSar)}$), 2.40–2.17 (m, 72H (2n), γ-C*H*$_{2(pGlu)}$), 2.10–1.79 (m, 74H (2n), β-C*H*$_{2(pGlu)}$), 1.42–1.38 (m, 5H, residual PG), 0.86–0.80 (s, 7H, -C*H*$_{3(NPA)}$). HFIP-GPC, relative to PMMA standards. pGlu(OH)$_{36}$-*b*-pSar$_{171}$ (P3): M_n = 37.9 kg/mol, M_w = 59.1 kg/mol; $Đ$ = 1.56.

Synthesis of (pGlu(Mod)-b-pSar) PGlu(OH)$_{36}$-*b*-pSar$_{171}$ (P3) (100 mg; 5.95 µmol; 1.0 eq.) was dissolved in 2.0 mL of anhydrous DMSO and 0.5 mL DMF.

Subsequently, *N,N,N′,N′*-tetramethyl-*O*-(1*H*-benzotriazol-1-yl)uronium hexafluorophosphate (HBTU) (135 mg, 357 µmol, 60 eq.), 1-hydroxy benzotriazole (HOBt) (48.2 mg; 357 µmol; 60 eq.), DIPEA (75.9 µL, 446 µmol, 75 eq.), 3-azidopropylamine (1.2 mg, 11.9 µmol, 2.0 eq.) and 4-((6-hydroxyhexyl)oxy)benzonitrile (156 mg, 714 µmol, 60 eq.) were added. The reaction mixture was stirred for 3 days at room temperature. For purification, the reaction mixture was diluted with DMSO and dialyzed (MWCO 3.5 kDa) against DMSO followed by MilliQ water. Upon lyophilization, cyano- and azide-modified NPA-pGlu(Mod)$_{36}$-*b*-pSar$_{171}$-Ac (P4) was obtained as a white solid (60 mg, 43%), with a cyano-grafting efficiency of 52%, as determined by ^{1}H NMR. ^{1}H NMR. pGlu(Mod)$_{36}$-*b*-pSar$_{171}$ (P4) (400 MHz, DMSO-*d*$_6$), δ [ppm] = 8.17−7.89 (b s, 11H (1u, 1v, 1w), CON*H*$_{(pGlu)}$), 7.83−7.60 (b s, 37H (2v), -CNCCC*H*$_{(arom.)}$), 7.17−6.91 (b s, 37H (2v), -OCC*H*$_{(arom.)}$), 4.53−3.71 (m, 436H (2m, 1u, 5v, 1w), α-C*H*$_{(pGlu)}$, α-C*H*$_{2(pSar)}$, -OC*H*$_2$, -COOC*H*$_2$), 3.05−2.64 (m, 513H (2m), -C*H*$_{3(pSar)}$), 2.04−1.09 (m, 246H (8u, 12v, 4w), ß-C*H*$_{2(pGlu)}$, γ-C*H*$_{2(pGlu)}$, -C*H*$_2$-),. HFIP-GPC, relative to PMMA standards. pGlu(Mod)$_{36}$-*b*-pSar$_{171}$ (P4): M_n = 53.1 kg/mol, M_w = 74.8 kg/mol; $Đ$ = 1.41. FT-IR. pGlu(Mod)$_{36}$-*b*-pSar$_{171}$ (P4) (ATR unit) $\tilde{\nu}$ [cm^{-1}] = 2936 (C-H), 2871 (C-H), 2223 (CN), 2100 (N$_3$), 1731 (CO, ester), 1646 (CO, amide).

Synthesis of poly(sarcosine) pSar macroinitiators were prepared as reported previously.[42] Sarcosine NCA (1.04g; 90.6 mmol; 200 eq.), was dissolved in 10 mL dry DMF and *N*-boc-1,2-diaminoethane (7.17 µL; 45.2 µmol; 1.0 eq.) was added *via* stock solution in DMF. The clear, colorless solution was stirred at room temperature and the reaction was completed after three days, as monitored by FT-IR-spectroscopy. The sarcosine amino terminus was quenched by addition of acetic anhydride (43 µL; 452 µmol; 10 eq.) and DIPEA (154 µL; 906 µmol; 20 eq.). The solution was allowed to stir for an additional day at room temperature. Precipitation in diethyl ether yielded *N*-boc-protected poly(sarcosine) (P5) as a colorless solid (610 mg, 95%). For removal of the Boc protection group, *N*-Boc-pSar (P5) was dissolved in a mixture of (1:1) TFA/H$_2$O and stirred at 0 °C for 3 h. The clear yellow solution was dialyzed against aqueous NaHCO$_3$ and MilliQ water (MWCO 3.5 kDa) for 2 days each. The polymer was lyophilized from water and obtained as a white powder (455 mg, 71%). The chain length of the pSar block was determined by HFIP-GPC with pSar standards (pSar$_{140}$).[39] ^{1}H NMR. *N*-Boc-pSar$_p$-Ac (P5) (400 MHz, DMSO-*d*$_6$), *δ* [ppm] = 4.56−3.78 (m, 381H (2p), α-C*H*$_{2(pSar)}$), 3.10−2.68 (m, 586H (3p), -C*H*$_{3(pSar)}$), 1.40−1.33 (s, 9H, -C*H*$_{3(Boc)}$). NH$_2$-pSar$_{140}$ (P6) (400 MHz, DMSO-*d*$_6$), *δ* [ppm] = 4.50−3.79 (m, 280H (2p), α-C*H*$_{2(pSar)}$), 3.10−2.60

(m, 420H (3p), -C$H_{3(pSar)}$). HFIP-GPC, relative to PMMA standards. NH_2-pSar_{140} (P6): M_n = 28.7 kg/mol, M_w = 34.5 kg/mol; $Đ$ = 1.20.

Synthesis of poly(sarcosine)-block-poly(γ-tert-butyl-L-glutamic acid) (pSar-b-pGlu(OtBu) The synthesis of pSar-*b*-pGlu(O*t*Bu) was adapted from literature and modified.[34,42] pSar (pSar_{140}, 110 mg; 10.9 µmol, 1.0 eq.) was weighed into a pre-dried Schlenk-flask and dried *via* azeotropic distillation with toluene. Next, the macroinitiator was dissolved in dry 1.0 mL DMF (freshly amine-purified by freeze-thaw cycles), cooled to 0 °C under N_2 atmosphere, and Glu(O*t*Bu) NCA (50 mg, 21.8 µmol, 20 eq.) was added *via* stock solution in DMF. Absolute THF was added to ensure polymerization in a THF/DMF (1:2) mixture. Upon completed monomer consumption, as monitored by FT-IR, pentafluorphenyl-4-azidobutanoate (6.44 mg; 21.8 µmol, 2.0 eq.) and DIPEA (7.4 µL; 43.6 µmol; 4.0 eq.) were added and the solution was stirred at room temperature for 18 h. To quench residual free end-groups, acetic anhydride (10.4 µL; 109 µmol; 10 eq.) and DIPEA (37.1 µL; 218 µmol; 20 eq.) were added and the solution was stirred for 1 day. Precipitation in diethyl ether yielded Ac-pSar_{140}-*b*-pGlu(O*t*Bu)$_{20}$-N_3 (P7) as a colorless solid (144 mg, 93%). ^{1}H NMR. pSar_{140}-*b*-pGlu(O*t*Bu)$_{20}$ (P7-A) (400 MHz, CD_2Cl_2), δ [ppm] = 8.61−8.03 (b s, 14H (1q), -CON*H*), 4.40−3.78 (m, 292H (1q, 2p), α-C$H_{(pGlu)}$, α-C$H_{2(pSar)}$), 3.14−2.80 (m, 420H (3p), -C$H_{3(pSar)}$), 2.66−1.95 (m, 72H, ß-C$H_{2(pGlu)}$, γ-C$H_{2(pGlu)}$), 1.53−1.35 (s, 172H, -C$H_{3(pGlu)}$). Ac-pSar_{140}-*b*-pGlu(O*t*Bu)$_{15}$-N_3 (P7-B) (400 MHz, CD_2Cl_2), δ [ppm] = 8.61−8.03 (b s, 8H (1q), -CON*H*), 4.40−3.78 (m, 284H (1q, 2p), α-C$H_{(pGlu)}$, α-C$H_{2(pSar)}$), 3.14−2.80 (m, 420H (3p), -C$H_{3(pSar)}$), 2.66−1.95 (m, 65H, ß-C$H_{2(pGlu)}$, γ-C$H_{2(pGlu)}$), 1.53−1.35 (s, 133 H, -C$H_{3(pGlu)}$). HFIP-GPC, relative to PMMA standards. pSar_{140}-*b*-pGlu(O*t*Bu)$_{20}$ (P7-A): M_n = 30.0 kg/mol, M_w = 39.3 kg/mol; $Đ$ = 1.31. pSar_{140}-*b*-pGlu(O*t*Bu)$_{15}$ (P7-B): M_n = 30.3 kg/mol, M_w = 40.7 kg/mol; $Đ$ = 1.34.

Synthesis of poly(sarcosine)-block-poly(L-glutamic acid) (pSar-b-pGlu(OH) For removal of the *tert*-butyl protecting group, pSar_p-*b*-pGlu(O*t*Bu)$_q$ (P7) was dissolved in a mixture of (45:45:5:5) DCM/TFA/TIPS/water and stirred for 3 h at 0 °C. Polymers were precipitated in ether, centrifuged (4000 rpm, 10 min, 4 °C) and the precipitate was dialyzed against aqueous $NaHCO_3$ solution and MilliQ water (MWCO 3.5 kDa), followed by lyophilization. The procedure was repeated until successful deprotection was verified by the absence (or presence of minor traces) of the *tert*-butyl group by ^{1}H NMR. ^{1}H NMR. pSar_{140}-*b*-pGlu(OH)$_{20}$ (P8-A) (400 MHz, D_2O), δ [ppm] = 4.55−4.02 (m, 295H (1q, 2p), α-C$H_{(pGlu)}$, α-C$H_{2(pSar)}$), 3.13−2.77 (m, 420H (3p), -C$H_{3(pSar)}$), 2.58−2.25 (m, 36H (2q), γ-C$H_{2(pGlu)}$), 2.20−1.85

(m, 38 H (2q), ß-C$H_{2(pGlu)}$). pSar$_{140}$-*b*-pGlu(OH)$_{15}$ (P8-B) (400 MHz, D_2O), δ [ppm] = 4.55–4.02 (m, 293H (1q, 2p), α-C$H_{(pGlu)}$, α-C$H_{2(pSar)}$), 3.13–2.77 (m, 420H (3p), -C$H_{3(pSar)}$), 2.48–2.22 (m, 29H (2q), γ-C$H_{2(pGlu)}$), 2.12–1.83 (m, 30H (2q), ß-C$H_{2(pGlu)}$). HFIP-GPC, relative to PMMA standards. pSar$_{140}$-*b*-pGlu(OH)$_{20}$ (P8-A): M_n = 28.2 kg/mol, M_w = 35.6 kg/mol; $Đ$ = 1.26. pSar$_{140}$-*b*-pGlu(OH)$_{15}$ (P8-B): M_n = 30.9 kg/mol, M_w = 54.1 kg/mol; $Đ$ = 1.75.

Synthesis (pSar-b-pGlu(Mod) PSar$_{140}$-*b*-pGlu(OH)$_{20}$ (P8-A) (90 mg; 7.18 µmol; 1.0 eq.) was dissolved in 2.0 mL of anhydrous DMSO and HBTU (163 mg, 431 µmol, 60 eq.), HOBt (58.2 mg, 431 µmol, 60 eq.), DIPEA (85.5 µL, 503 µmol, 70 eq.) and 4-(2-aminoethoxy)benzonitrile (46.6 mg, 287 µmol, 40 eq.) were added subsequently. The reaction mixture was stirred for 3 days at room temperature. Repetitive precipitation in acetone (3800 rpm, 15 min, 4 °C) yielded statistically modified Ac-pSar$_{140}$-*b*-pGlu(Mod)$_{20}$-N_3 (P9-A) as a colorless solid (77.5 mg, 70%). Successful modification was verified by FT-IR spectroscopy and DOSY NMR. Grafting efficiencies of 65% and 100% were obtained for P9-A and P9-B, as determined by ^{1}H NMR. ^{1}H NMR. pSar$_{140}$-*b*-pGlu(Mod)$_{20}$ (P9-A) (400 MHz, DMSO-d_6), δ [ppm] = 8.28–7.90 (b s, 23H (2r, 1s), CON$H_{(pGlu)}$), 7.83–7.63 (b s, 26H (2r), -CNCCC$H_{(arom.)}$), 7.14–6.98 (b s, 26H (2r), -OCC$H_{(arom.)}$), 4.56–3.70 (m, 310H (3r, 1s, 2p), α-C$H_{(pGlu)}$, α-C$H_{2(pSar)}$, -OCH_2), 3.47–3.37 (m, 21H (2r), -CONHC$H_{2(pGlu)}$), 3.08–2.62 (m, 420H (2p), -C$H_{3(pSar)}$), 2.29–1.53 (m, 117H (4r, 4s), ß-C$H_{2(pGlu)}$, γ-C$H_{2(pGlu)}$). pSar$_{140}$-*b*-pGlu(Mod)$_{15}$ (P9-B) (400 MHz, DMSO d_6), δ [ppm] = 8.28–7.90 (b s, 26H (2r, 1s), CON$H_{(pGlu)}$), 7.83–7.63 (b s, 30H (2r), -CNCCC$H_{(arom.)}$), 7.14–6.98 (b s, 29H (2r), -OCC$H_{(arom.)}$), 4.56–3.70 (m, 318H (3r, 1s, 2p), α-C$H_{(pGlu)}$, α-C$H_{2(pSar)}$, -OCH_2), 3.08–2.62 (m, 420H (2p), -C$H_{3(pSar)}$), 2.29–1.53 (m, 76H (4r, 4s), ß-C$H_{2(pGlu)}$, γ-C$H_{2(pGlu)}$). FT-IR. pSar$_{140}$-*b*-pGlu(Mod)$_{20}$ (P9-A) (ATR unit) $\tilde{\nu}$ [cm^{-1}] = 2936 (C-H), 2871 (C-H), 2223 (CN), 1640 (CO, amide). HFIP-GPC, relative to PMMA standards. pSar$_{140}$-*b*-pGlu(Mod)$_{20}$ (P9-A): M_n = 71.3 kg/mol, M_w = 113.2 kg/mol; $Đ$ = 1.58. pSar$_{140}$-*b*-pGlu(Mod)$_{15}$ (P9-B): M_n = 47.9 kg/mol, M_w = 61.5 kg/mol; $Đ$ = 1.28.

Preparation of Photocleavable Core Cross-Linked Polymeric Micelles

Cyano-group-modified pGlu(Mod)-*b*-pSar was dissolved in DMSO at a concentration of 5.0 g·L^{-1}. The clear solution was dialyzed against MilliQ water (MWCO 3.5 kDa), filtered (GHP 450) and concentrated to the 5.0 g·L^{-1} by spin filtration (Amicon Ultra, MWCO 3 kDa), yielding the micelle solution. For cross-linking, ruthenium complexes were dissolved in methanol (10 g·L^{-1}) and added at

equimolar concentration with respect to the number of nitrile groups. The reaction mixture was protected from light and kept at 50 °C until completed ligand exchange, as monitored optically (PCCPM-1: color change from red to yellow; PCCPM-2: dark blue to purple) and *via* UV-Vis spectroscopy (PCCPM-1: λ_{max} = 482 nm to 420 nm; PCCPM-2: λ_{max} = 590 nm to 550 nm). To remove residual cross-linker and not cross-linked polymer, the particle solution was diluted with a mixture of ethanol/water (1:1) and purified by repetitive spin filtration (Amicon Ultra, MWCO 100 kDa) and dilution steps with MilliQ water until no residual free polymer was detectable in HFIP-GPC. In cases where labelling was required for biological evaluation, sulforhodamine-B-PEG_4-dibenzocyclooctine (DBCO) (0.4 eq. per polymer) was added, and the solution stirred for 3 days before core cross-linking was performed. Labelled micelles were purified from free dye by repetitive spin filtration (Amicon Ultra, MWCO 10 kDa) and dilution steps. Successful removal of free dye was ensured by HFIP-GPC. Final particle solutions could be stored in the absence of light at 4 °C.

Photocleavage

Light-induced cleavage of PCCPMs was performed using high brightness LEDs with narrow emission spectra of blue (λ_{max} = 455 nm), green (λ_{max} = 535 nm), or red orange (λ_{max} = 620 nm) light. Particle solutions were transferred into sealed transparent vials, diluted with MilliQ water to a concentration of approx. 0.1 $g \cdot L^{-1}$ and irradiated with LED light. For time-dependent UV-Vis measurements, aliquots were taken and analyzed. For HFIP-GPC analysis, aliquots were taken, concentrated *in vacuo* and analyzed. The following LEDs were used: Blue LED: (λ_{max} = 455 nm), Osram, High-Brightness-LED, OSLON SSL 80 Series, Blue, 455 nm, 80°, 1A. Green LED: (λ_{max} = 535 nm), Cree, High-Brightness-LED, XLamp XP-E2, Green, 535 nm, 135°, 114 lm, 1A. Red orange LED: (λ_{max} = 620 nm), Cree, High Brightness SMD, Red Orange, 87.4 lm.

Biologic Evaluation

Cell Viability. To measure cellular viability, the AlamarBlue assay was performed according to manufacturer's specifications as recently described in detail by Ernst *et al.* with minor modifications.[51] Briefly, 40'000 HuH-7 tumor cells were seeded in 96-well-plates in 200 µl cell culture medium per well. After 24 h, cells were subjected to the indicated treatment. After incubation with PCCPMs or ruthenium(II) complex at 10 µM ruthenium(II) complex 1 or 2 for 24h, cells were either exposed to light (455 nm, 5 minutes; 535 nm, 15 minutes) or kept in the

dark to avoid light exposure. To measure cellular viability, medium was exchanged for medium with 10% AlamarBlue (Invitrogen, Life Technologies Corp., Eugene, OR, USA) and the cells were incubated for 4 h at 37°C before recording the fluorescence on a fluorescence microplate reader (Fluoroskan Ascent Microplate reader, Thermo Fisher Scientific GmbH, Rockford, USA). Results were given as relative values using a 538 nm excitation filter and a 600 nm emission filter, normalized to the respective control (100%).

Chicken Chorioallantoic Membrane Assay. White leghorn hens' eggs (Bio-Aufzucht LSL Rhein-Main GmbH, Dieburg, Germany) were placed horizontally in an incubator (Brutmaschinen-Janeschitz GmbH, Hammelburg, Deutschland) at 37.5 °C. After removal of 6 mL albumin by aspiration on day 3 of incubation the eggshell was opened and partly removed with sterilized scissors to expose the chorioallantoic membrane (CAM). Between further experiments the aperture was constantly covered with PARAFILM® (Bemis Company Inc., Neenah, Wisconsin, USA) to avoid evaporation. On day 13 of cultivation, 500 µL of PCCPM-nanoparticles were intravascularly injected using a sterile-single-use-syringe (B. Braun Melsungen AG, Meldungen, Germany) with a 30G x ½" needle (BD Microlance™ 3, Becton, Dickinson and Company United, Louth, Ireland). 19 eggs were investigated. Death of the embryo within the timeframe of observation as well as a lack of particle circulation due to paravasal injection were reasons for a dropout from further investigation. After intravascular application of the sulforhodamine-B-labeled nanoparticles, *in vivo* fluorescent microscopy (BXFM intravital microscope (Olympus BXFM, OLYMPUS DEUTSCHLAND GmbH, Hamburg, Germany) was performed and repeated after 3 h and 24 h after the application of the nanoparticles respectively. By using the Cy3 Filter (Ex: 545 nm; Em: 525 nm), video sequences of 20 s each were taken in a representative region of interest on the CAM using the microscope camera system (CAM-XM10, OLYMPUS DEUTSCHLAND GmbH, Hamburg, Germany). The video sequences were later analyzed offline. After blinding, video sequences were investigated repetitively three times. As the number of particles in the vascular system did not allow a sufficient quantitative analysis, we used the following numerical analogue scale: 5 = intravascular PCCPMs can be detected ubiquitously; 4 = intravascular PCCPMs can be detected predominantly; 3 = intravascular PCCPMs can be detected occasionally; 2 = PCCPMs can be detected; 1 = no PCCPMs can be detected.

Staining and Histological Analysis. Histology was performed 24 h after intravascular injection of sulforhodamine-B-labeled PCCPMs. Brain, heart, liver, and kidney were put in a formalin solution (VWR International bvba, Leuven, Belgium) 4% (v/v) in PBS and embedded in paraffin (Roti® Plast, Carl Roth GmbH + Co. KG, Karlsruhe, Germany) on the following day. After embedding the samples in paraffin, the fixed preparations were cut into slides with the microtome (Leica CM1900, Leica Biosystems Nussloch GmbH, Nußloch, Germany) and then transferred to the specific staining/immunohistochemical analysis, respectively. Samples were dewaxed by incubation in xylene solutions (AppliChem GmbH, Darmstadt, Germany) with descending concentrations (100%, 90%, 80%, 70%). Afterwards, the slides were transferred for 5 min in purified water. Subsequently, 25 µL of VECTASHIELD® HardSet™ Antifade Mounting with 4',6-diamidino-2-phenylindole (DAPI) (Vector Laboratories, Inc., Burlingame, CA, USA) was pipetted onto the histological specimen, which was subsequently covered with a cover slip. Hemalum-Eosin staining was also performed to allow light microscopical evaluation of the tissue samples. After dewaxing samples were put in in acidic hemalum solution acc. to Mayer (Carl Roth GmbH + Co. KG, Karlsruhe, Germany) for 5 min. Afterwards, blueing was performed for 10 min under running tap water. The sample was then transferred for 2 min in purified water again before being transferred to 0.5% eosin solution (Carl Roth GmbH + Co. KG, Karlsruhe, Germany) for 2-3 min. After re-rinsing under tap water specimens were transferred in isopropanol solution of ascending concentration (1-2 min in 80% isopropanol (Shell Chemicals Europe B.V., Rotterdam/Pernis, Netherlands) 1-2 min 90% isopropanol, 3 min 100% isopropanol) and for 2 x 5 min in 100% xylene. Finally, the specimen was covered with Eukitt® inclusion agent (Sigma-Aldrich, St. Louis, Missouri, USA). After preparation histological samples were analyzed using fluorescence microscopy (Nikon Eclipse TE2000, Nikon Corporation, Chiyoda, Japan). The inbuilt DAPI filter (Ex:340-380 nm, Em:435-485 nm) was used to identify stromal tissue after an image in DAPI staining was taken, the filter was subsequently switched to Cy3 (Ex:530-560, Em:573-648nm) and an image was taken in this staining respectively. Both images were merged using Nikon's imaging software NIS-Elements (Nikon Corporation, Chiyoda, Japan). The images were then blinded for analysis and the number of nanoparticles within the respective stromal tissue was qualitatively analyzed as follows. 5 = PCCPMs can be detected ubiquitously; 4 = PCCPMs can be detected predominantly; 3 = PCCPMs can be detected in

disseminated locations; 2 = PCCPMs can be detected occasionally; 1 = PCCPMs can be detected; 0 = no PCCPMs can be detected.

Data Management and Statistical Analysis. Data sets were managed using Microsoft Excel (Microsoft Corporation, Redmont, WA, USA) as well as Graph Pad Prism (GraphPad Software, La Jolla, CA, USA). Differences between individual groups in the AlamarBlue assay, the particle quantifications in both *in vivo* microscopy and the fluorescence microscopy were evaluated by two-way ANOVA. Differences $p < 0,05$ were considered significant.

Results and Discussion

The described photocleavable core cross-linked polymeric micelles are based on polypept(o)ides, which were synthesized by sequential nucleophilic ring-opening polymerization of the corresponding NCAs.[33,34] As shown in Scheme 1, the block copolymers of poly(*tert*-butyl-l-glutamic acid)-*block*-polysarcosine (pGlu(O*t*Bu)-*b*-pSar) were prepared starting from pGlu(O*t*Bu) (P1) followed by sequential monomer addition of sarcosine NCA. After end-capping with acetic anhydride, the *tert*-butyl protecting-group was removed from pGlu(O*t*Bu)-*b*-pSar (P2) yielding pGlu(OH)-*b*-pSar (P3). Upon purification by precipitation and dialysis, the pGlu(OH)-block was modified with aromatic cyano-groups that allow for coordination to the ruthenium complexes as well as with 3-azidopropylamine for optional dye conjugation *via* azide-alkyne click chemistry, which resulted in pGlu(Mod)-*b*-pSar (P4).[52,53]

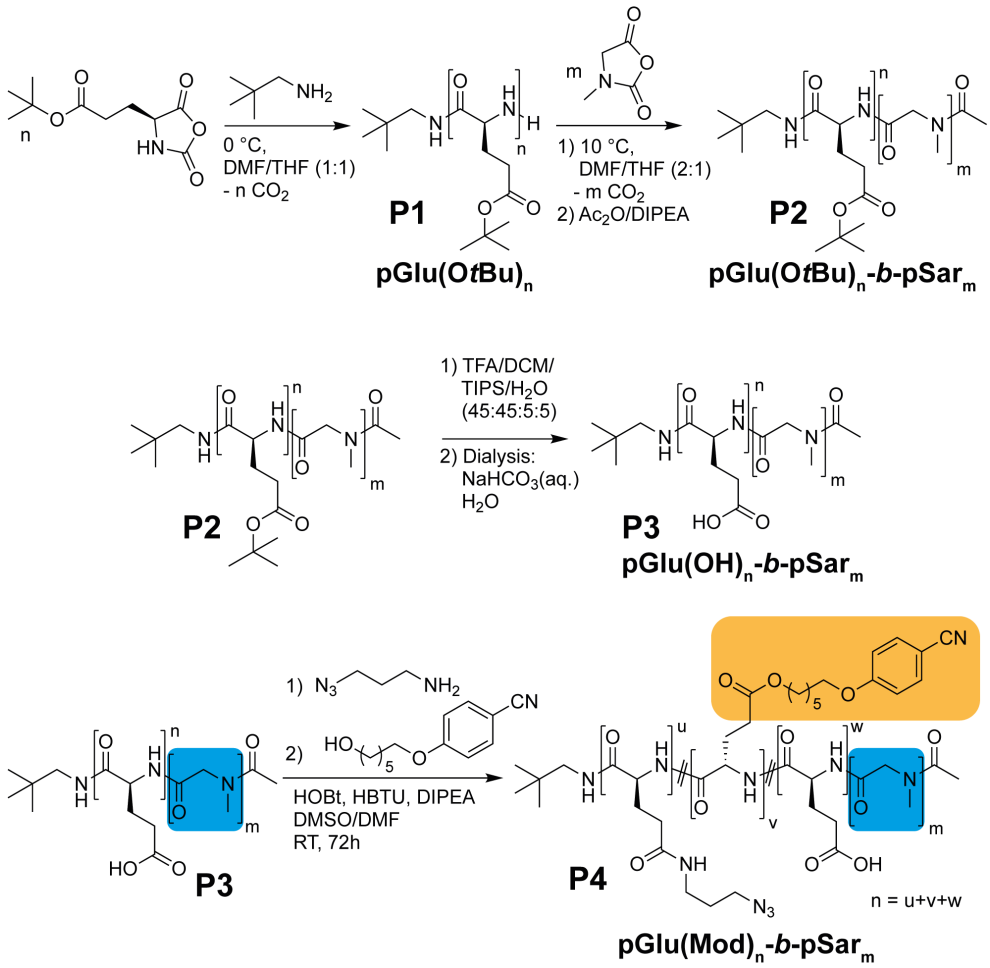

Scheme 1. Polymer synthesis and post polymerization modification reactions.

As shown in Figure 1A, symmetric and monomodal molecular weight distributions were obtained for pGlu(O*t*Bu) (P1), pSar-*b*-pGlu(O*t*Bu) (P2), and pGlu(Mod)-*b*-pSar (P4) by GPC in HFIP. A distinct shift in the elution volume maximum can be detected after the addition of the second block accounting for the living nature of the NCA polymerization, which is also reflected by the narrow dispersities of 1.16 and 1.20 for P1 and P2.[35,36,54] Moreover, the chain lengths of X_n = 36 for pGlu(O*t*Bu) and X_m = 171 for pSar, which were determined by end-group analysis in ^{1}H NMR are in well agreement with the calculated monomer-to-initiator ratios as summarized in Table 1.

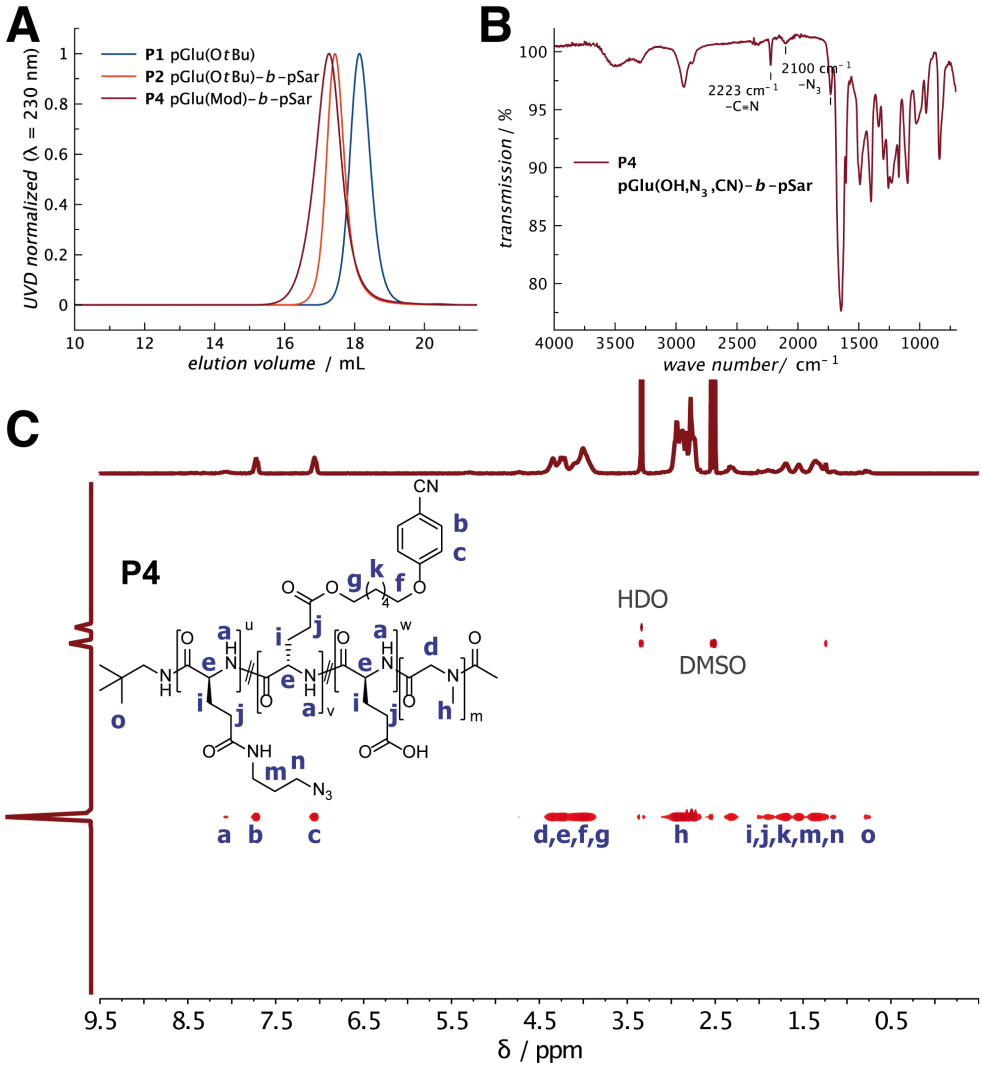

Figure 1. Polymer Analysis. (**A**) HFIP-GPC displays monomodal and symmetric molecular weight distributions for P1, P2, and P4; (**B**) FT-IR spectroscopy confirms successful polymer modification with azide and nitrile groups; (**C**) DOSY NMR spectroscopy in DMSO-d_6 shows only one diffusing polymer species with all signals aligned in one horizontal axis.

After modification with 4-(6-hydroxyhexyloxy)-benzonitrile and 3-azidopropylamine, a grafting density of 52% was determined by ^{1}H NMR analysis. Besides larger molecular weights only a slightly increased dispersity

was obtained by GPC. The successful backbone modification reaction was then verified by DOSY NMR spectroscopy. Here, only one diffusing polymer species was detected with all signals aligned in one horizontal axis (Figure 1C). The presence of the conjugated nitrile- and azide-groups was confirmed by FT-IR spectroscopy where distinct peaks at 2223 cm^{-1} (-C≡N) and 2100 cm^{-1} (-N_3), as well as peaks of the associated ester bond (1731 cm^{-1}) are visible (Figure 1B).

Table 1. Analytical results of the polymer synthesis and post-polymerization modification reactions.

polymer	X_n (pGlu)[a]	X_n (pSar)[a]	M_n[b] / kDa	M_w[b] / kDa	$Đ$[b] /kDa	CN-grafting
P1, pGlu(O*t*Bu)	36	-	19.7	22.9	1.16	-
P2, pGlu(O*t*Bu)-*b*-pSar	36	171	44.0	52.9	1.20	-
P3, pGlu(OH)-*b*-pSar	36	171	37.9	59.1	1.56	-
P4, pGlu(Mod)-*b*-pSar	36	171	53.1	74.8	1.41	52%

[a] ^{1}H NMR end-group analysis, [b] relative to PMMA standards.

Polymeric micelles were formed by self-assembly of the amphiphilic nitrile-modified polypept(o)ide pGlu(Mod)-*b*-pSar (P4) using the solvent switch-method from DMSO to water, as illustrated in Figure 2. After solvent exchange by dialysis was completed, the polymeric micelles were core cross-linked by the addition of the respective Ruthenium complex and purified by ultrafiltration. The progress of the ligand exchange reaction, and thus the proceeding of the cross-linking could easily be monitored by eye (Figure S3) and UV-Vis spectroscopy (Figure 2B).

For *cis*-diaquabis(2,2'-bipyridine)-ruthenium (II) bis(hexafluorophosphate) ([Ru(bpy)$_2$(H_2O)$_2$] (PF_6)$_2$; Ru-CPX-1), a color change from red to bright yellow was observed that corresponds to a blue-shift in the wavelength of the MLCT from 482 nm to 420 nm. Similarly, for *cis*-diaquabis(2,2'-biquinoline)-ruthenium (II) bis(hexafluorophosphate) ([Ru(biq)$_2$(H_2O)$_2$] (PF_6)$_2$; Ru-CPX-2), which has a larger π-system, a color change from dark blue to purple could be seen, which refers to a change in the wavelength of the MLCT from 592 nm to 548 nm upon ground state exchange of the two aqua-ligands by nitrile-ligands.[55,56] When analyzed by DLS, polymeric micelles showed a hydrodynamic diameter of 41 nm and a narrow PDI of 0.058. As shown in Figure 2C, this was neither affected by cross-linking with [Ru(bpy)$_2$(H_2O)$_2$] (PF_6)$_2$ (PCCPM-1) nor by [Ru(biq)$_2$(H_2O)$_2$] (PF_6)$_2$ (PCCPM-2).

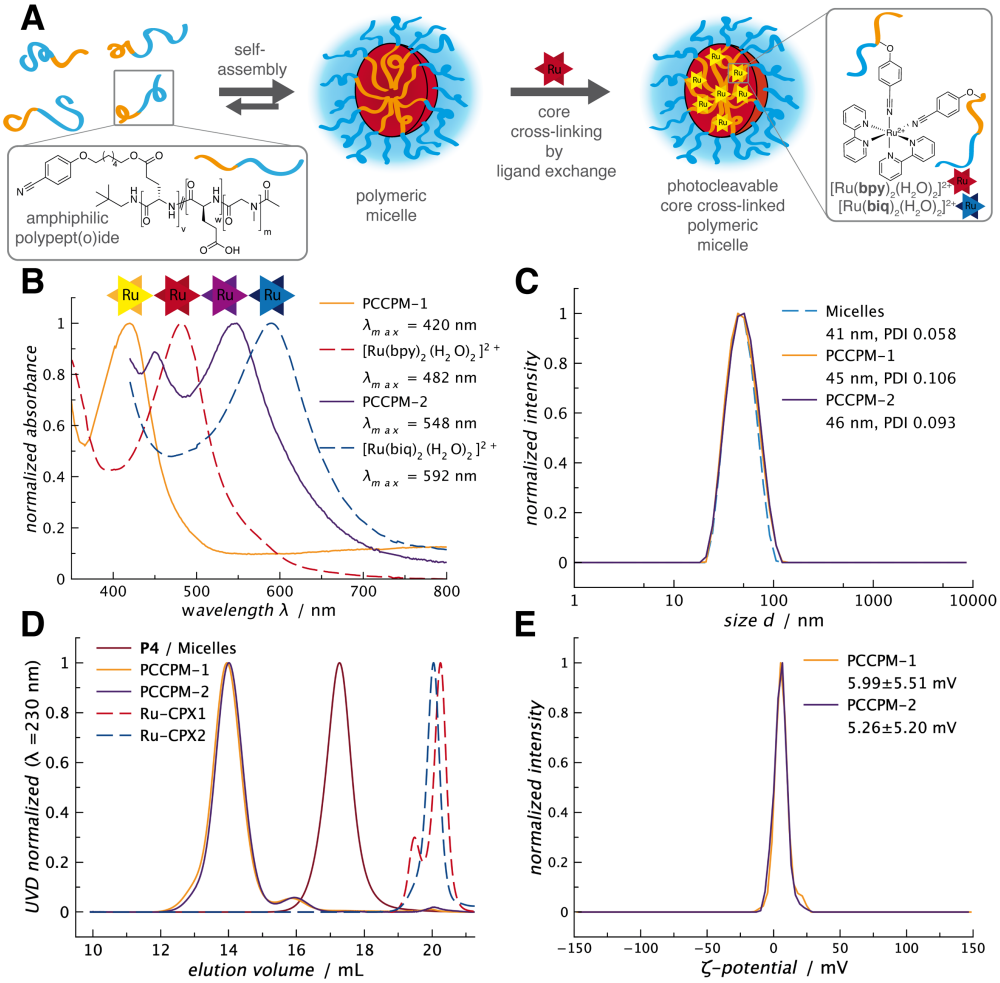

Figure 2. Nanoparticle characterization. (**A**) Schematic illustration of the self-assembly and core cross-linking process; (**B**) UV-Vis spectroscopy for ruthenium complexes and core cross-linked micelles with indicated λ_{MLCT} values; (**C**) DLS of micelles and PCCPMs; (**D**) HFIP-GPC demonstrates stable cross-linking after incubation for ≥1 h; (**E**) Neutral ξ-potentials account for efficient shielding by the pSar corona.

After purification by ultrafiltration the particle structure remained stable even in the GPC with HFIP, whereby no significant traces of free polymer or ruthenium complex could be detected after incubation for at least one hour (Figure 2D). The particle stability was further confirmed by DLS in human plasma, following the technique introduced by Rausch *et al.*, whereby no aggregation could be detected

(Figure S4).[47] These results confirm the integrity of the proposed core cross-linked micellar structure demonstrating the suitable basis for smart drug delivery in which carrier disintegration solely follows internal or external stimuli.[57–59] When analyzed by solution nebulization inductively coupled plasma mass spectrometry (SN-ICP-MS), drug loading contents of 4.37 ± 0.18 and 4.34 ± 0.17 weight% were determined for both, PCCPM-1 ($[Ru(bpy)_2(H_2O)_2]$ $(PF_6)_2$) and PCCPM-2 ($[Ru(biq)_2(H_2O)_2]$ $(PF_6)_2$). Furthermore, neutral ξ-potentials were detected accounting for sufficient shielding by the pSar corona (Figure 2E). The results of the particle preparation are summarized in Table 2.

For Ruthenium-cross-linked polymeric micelles of pGlu(Mod)-*b*-pSar (P4), spherical morphologies with sizes well below 50 nm were detected by TEM and AFM analysis for both, PCCPM-1 and PCCPM-2, which corresponds well with the DLS data (Figure 3, Figure S7). With more detail, for PCCPM-2, narrow dispersities and small particle diameters of 20.2 ± 4.5 nm (PDI 0.05, no staining) and 22.8 ± 4.3 nm (PDI 0.03, negative staining) were derived from TEM image analysis (Figure S5, S6).

Table 2. Analytical results of the PCCPM preparation

particle	Ru-CPX	D_h / nm[a]	PDI[a]	Ru-CPX wt.%[b]	ξ-potential / mV[a]
Micelles	-	41	0.058	-	-
PCCPM-1	$[Ru(bpy)_2]^{2+}$	45	0.106	4.37 ± 0.18	5.99 ± 5.51
PCCPM-2	$[Ru(biq)_2]^{2+}$	46	0.093	4.34 ± 0.17	5.26 ± 5.20

[a] single-angle DLS at 173°, [b] ICP-Ms.

Given the fact that DLS is used to calculate the intensity weighted size distribution and the hydrodynamic diameter of a given particle solution, the smaller sizes determined by TEM analysis refer to the particle analysis in the dry state.[60,61] Moreover, the slightly smaller diameters detected for non-stained compared to negatively stained samples indicate that the ruthenium complex which primarily accounts for the transmission contrast mainly concentrates in the core of the particle confirming the illustrated core-shell structure.[20,62]

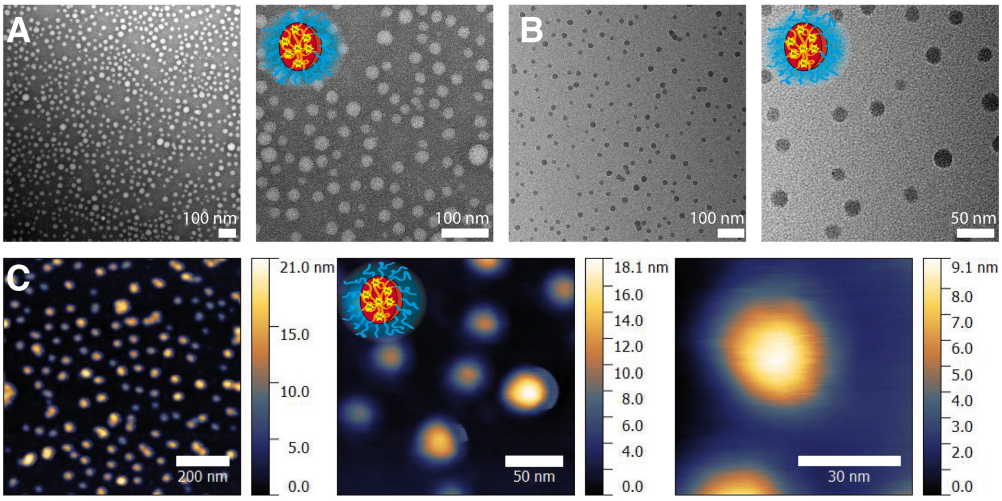

Figure 3. Particle analysis of PCCPMs by imaging techniques reveals small spherical structures. (**A**) TEM images (negatively stained with uranyl acetate); (**B**) TEM images of (non-stained); (**C**) AFM images with apparent height profiles.

Interestingly, when the aromatic nitrile-linker for the conjugation of the ruthenium complexes that was grafted to the polymer backbone was exchanged to a less flexible structure with only two instead of six methylene units, much larger micelles of 88 nm were detected by DLS (Figure 4, Table 3). Again, the overall size distribution was not changed after core cross-linking with $[Ru(bpy)_2(H_2O)_2]$ $(PF_6)_2$ or $[Ru(biq)_2(H_2O)_2]$ $(PF_6)_2$. However, further analysis by multi-angle DLS indicated an angle-dependency for these structures, pointing towards non-spherical morphologies (Figure S8). Finally, by imaging techniques, worm-like structures could be revealed for PCCPMs based on polymer P9-A. As shown in Figure 4D, the worm-like core cross-linked micelles displayed uniform widths of approx. 25 ± 3 nm (N = 27) with variable lengths (157 ± 83 nm; N = 90), accompanied by a fraction of small spherical structures (also see Figure S9, S10). The coexistence of worm-like and spherical structures was confirmed by cryo-TEM analysis (Figure 4B) and is further reflected in the GPC elugrams, whereby a fraction of very large species at or above the upper detection limit (12 mL) together with a smaller fraction (15 mL) have been detected for w-PCCPM-1 and w-PCCPM-2. Of note, no free polymer was detected accounting for core cross-linked micelles.

Table 3. Analytical results of the PCCPM preparation

particle	Ru-CPX	D_h / nm[a]	*PDI*[a]	*Ru-CPX wt.%*[b]
w-micelles	-	88	0.163	-
w-PCCPM-1	$[Ru(bpy)_2]^{2+}$	91	0.216	4.81 ± 0.11
w-PCCPM-2	$[Ru(biq)_2]^{2+}$	98	0.170	15.5 ± 0.34

[a] single-angle DLS at 173°, [b] ICP-MS.

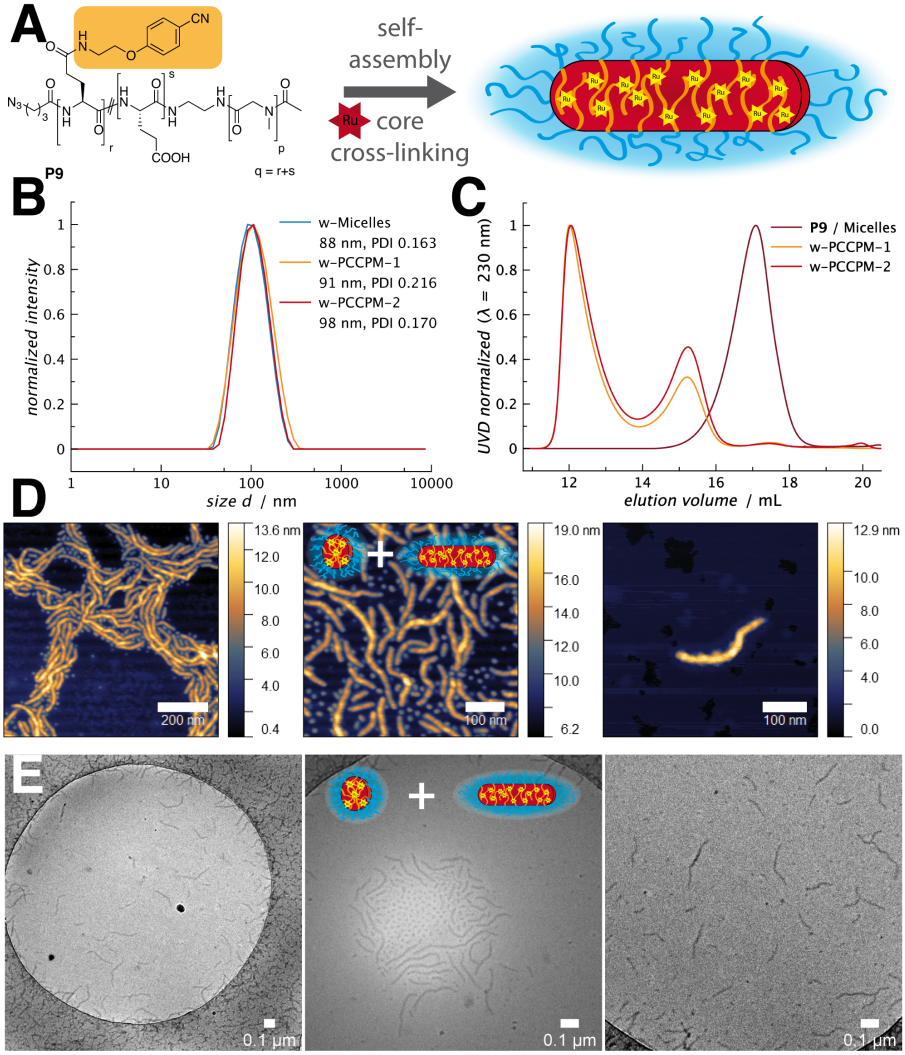

Figure 4. Analysis of worm-like core cross-linked polymeric micelles (w-PCCPMs). (**A**) The less flexible linker (orange) for ruthenium complex conjugation directs self-assembly to

worm-like micelles; (**B**) Cross-linking does not affect the size distribution in DLS analysis; (**C**) HFIP-GPC reveals the coexistence of small and large particles and absence of free polymer or leaking Ruthenium complex; (**D**) AFM images with apparent height profiles confirm the coexistence of spherical and worm-like particles; (**E**) Cryogenic TEM analysis confirms worm-like particles in solution.

Due to the strong absorbance of the aromatic rings, CD spectroscopy did not provide interpretable data on whether a change in the secondary structure is directing to the worm-like assemblies (data not shown). Nevertheless, reducing the chain lengths of the pGlu block while keeping the less flexible linker, again resulted in the formation of mainly small spherical core cross-linked polymeric micelles (Figure S11). In the uncharged state pGlu(OH) is known to adopt an α-helix secondary structure, which has been reported to facilitate the formation of spherical rather than worm-like structures.[63,64] A supramolecular stacking of the conjugated aromatic rings might thus account for the discovered 1-dimensional growth of the polymeric micelles derived from polymer P9-A.[65] Furthermore, the altered morphology could also be explained by differences in the hydrophobicity of the two linkers. Based on calculated *logP* values, the hexamethylene ester-linker is more hydrophobic than the ethylene amide-linker (*logP* = 2.84 and 1.04). This correlates well with $pSar_{140}$-*b*-$pGlu_{15}$ copolymers that have been modified with the two linkers, whereby aggregation starts earlier for the more hydrophobic copolymer when water is added to the polymer solution in DMSO (Figure S12).[66]

When exposed to light, the ruthenium(II) complexes have been reported to undergo photoinduced hydrolysis resulting in the cleavage of the nitrile-group coordination to the central metal-ion.[67,68] To verify this feature for ruthenium-based core cross-linked polymeric micelles, the nanoparticles were irradiated by narrow bandwidth high brightness LEDs, and the reaction was monitored by UV-Vis spectroscopy, as illustrated in Figure 5A. A blue LED ($\lambda \geq 455$ nm) was used to irradiate PCCPM-1 close to the local maximum of the nitrile-conjugated MLCT ($\lambda = 420$ nm). Within 60 s, a tremendous decrease of the local maximum could be observed, and the reaction was completed after irradiation for 5 minutes. The spectrum then matches the one of $[Ru(bpy)_2(H_2O)_2]^{2+}$, accounting for completed ligand exchange.

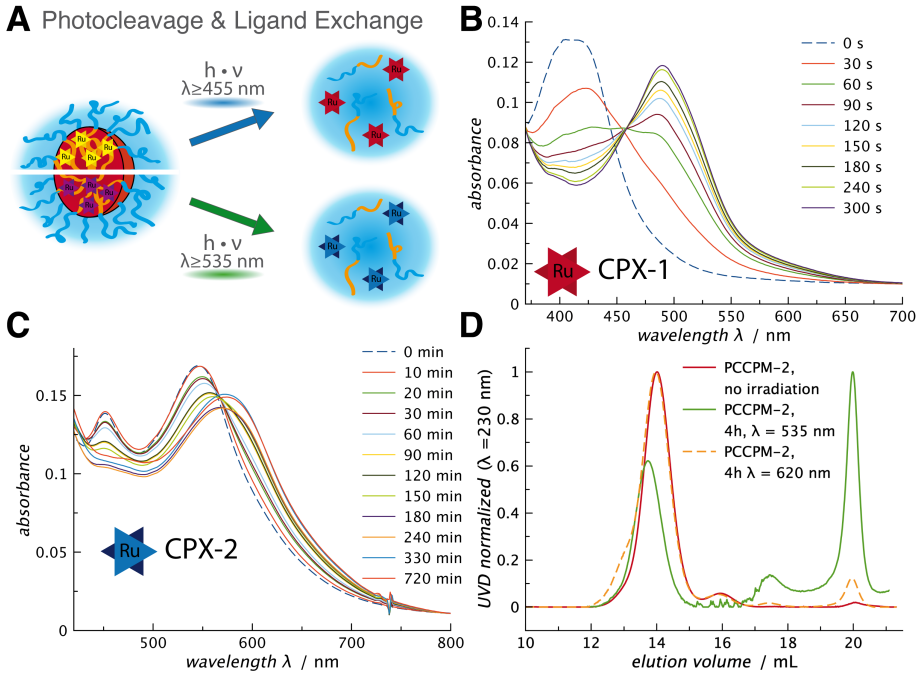

Figure 5. Analysis of the light-induced ligand exchange reaction. (**A**) Illustration of the performed irradiation experiments for PCCPM-1 and PCCPM-2; (**B**) UV-Vis spectroscopy of PCCPM-1 indicates completed cleavage within 300 s; (**C**) UV-Vis spectroscopy shows incomplete cleavage of PCCPM-2 after green-light irradiation for 12 h; (**D**) HFIP-GPC of PCCPM-2 before and after irradiation.

For PCCPM-2, a green LED ($\lambda \geq 535$ nm) was used to induce the cleavage reaction. As shown in Figure 5C, the wavelength of the local absorbance maximum shifts from 548 nm to 575 nm throughout the reaction, however, the MLCT peak does not recover the 590 nm of $[Ru(biq)_2(H_2O)_2]^{2+}$, which implies incomplete hydrolysis. Moreover, no significant change can be observed between 330 min and 720 min of irradiation. When analyzed by HFIP-GPC, released ruthenium complex (V = 20 mL) together with still intact particles (V = 14 mL) can be detected after 4 h of green light irradiation. When the photocleavage was performed with a red-orange LED (λ = 620 nm), progress was even slower (Figure S13) with hardly any cross-linker being released after 4 h. The distinctive kinetics of the photoinduced hydrolysis of PCCPM-1 and PCCPM-2 is also reflected by the reported quantum yields for the acetonitrile derivatives $[Ru(bpy)_2(CH_3CN)_2]^{2+}$ and $[Ru(biq)_2(CH_3CN)_2]^{2+}$. The light-induced exchange of the nitrile ligands by

irradiation at the MLCT follows a stepwise procedure involving intermediate monoaqua ruthenium(II) species.[69–71] For $[Ru(biq)_2(CH_3CN)_2]^{2+}$ quantum yields of $\varphi_{550\,nm}$ 0.15 and $\varphi_{550\,nm}$ 0.0014 indicate that the second ligand exchange is significantly slower which is in good agreement with our findings.[69] On the other hand, for $[Ru(bpy)_2(CH_3CN)_2]^{2+}$ high quantum yields of $\varphi_{450\,nm} = 0.22$ have been reported for the overall process yielding $[Ru(bpy)_2(H_2O)_2]^{2+}$, which is also reflected by the complete cleavage in less than 5 min for PCCPM-1.[70]

To investigate a potential application for photodynamic or photoactivated chemotherapy, PCCPMs were evaluated for their cytotoxicity *in vitro*, and the circulation behavior and organ distribution *in ovo* (Figure 6). When HuH-7 tumor cells were treated with photocleavable polymeric micelles containing 10 µM of $[Ru(bpy)_2(H_2O)_2]$ $(PF_6)_2$ (Ru-CPX-1) in the dark, a slight reduction in cell viability could be detected ($p < 0.01$), whereby the blue light irradiation ($\lambda \geq 455$ nm) did not induce significant cell death (Figure 6A). Moreover, the cell viability decreased only at very high concentrations above 200 µM for the micelle-free Ru-CPX-1 (Figure S14). These findings are congruent with the literature reporting $[Ru(bpy)_2(H_2O)_2]^{2+}$ as non-toxic, while it has been intensively studied as a model drug for binding of ruthenium(II) complexes to nucleosides or DNA.[72–75] Contrariwise, IC_{50} values of 25 µg·mL^{-1} and 2.5 µg·mL^{-1} have been reported for HeLa cells incubated with Ru-CPX-2 ($[Ru(biq)_2(H_2O)_2]$ $(PF_6)_2$) in the dark and with additional red light irradiation.[29] As shown in Figure 6B, however, HuH-7 cells did not respond to the treatment with $[Ru(biq)_2(H_2O)_2]$ $(PF_6)_2$ to the same extent. When treated with matching doses of 10 µM native Ru-CPX-2, no significant toxicity could be detected without irradiation, while the green light itself ($\lambda = 535$ nm) is the major cause of cell death for the irradiated samples (two-way ANOVA, $p < 0.0001$).

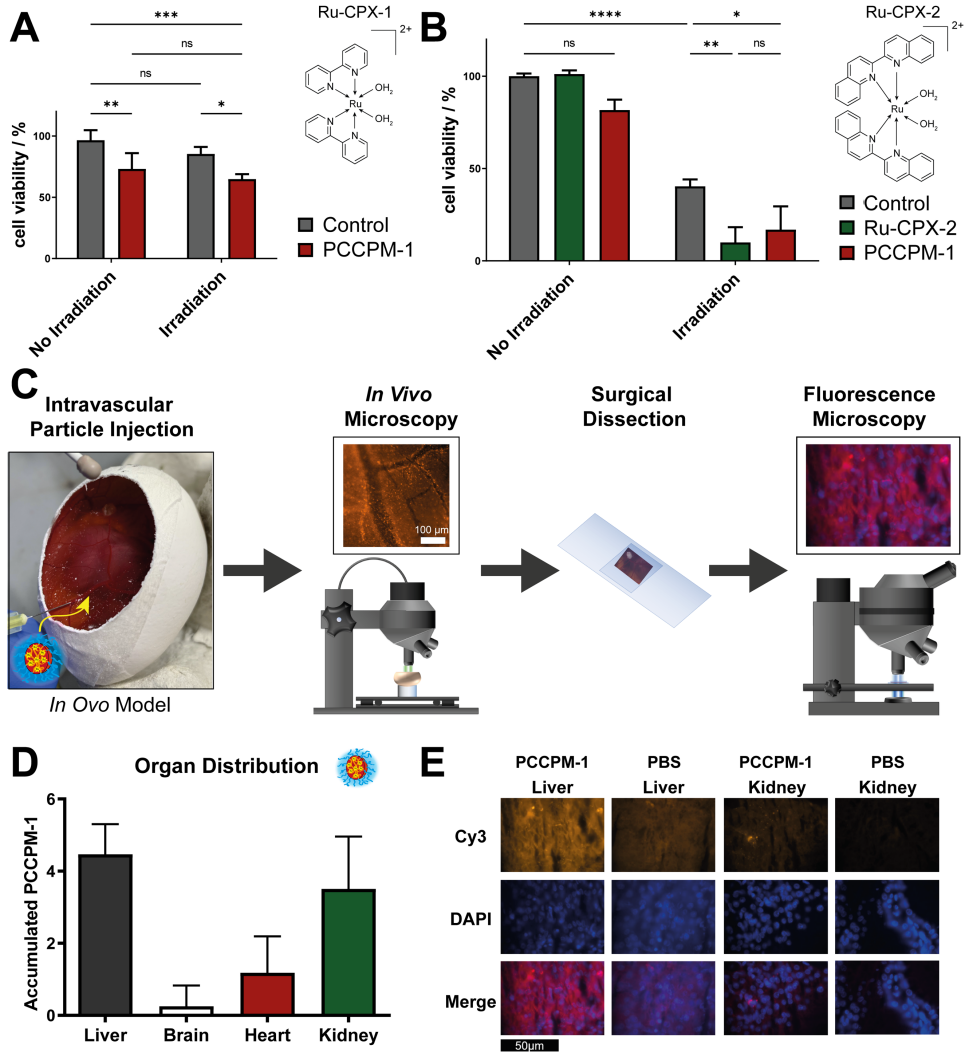

Figure 6. Biologic evaluation of PCCPMs. (**A**) Cell viability of HuH-7 tumor cells after incubation with NaCl (control) or PCCPM-1 at equivalent concentrations of 10 µM $[Ru(bpy)_2(H_2O)_2]$ $(PF_6)_2$, with and without irradiation ($\lambda \geq 455$ nm) for 5 minutes; (**B**) Cell viability of HuH-7 cells after incubation with NaCl (control), $[Ru(biq)_2(H_2O)_2]$ $(PF_6)_2$, and PCCPM-2 at equivalent concentrations of 10 µM $[Ru(biq)_2(H_2O)_2]$ $(PF_6)_2$,with and without irradiation ($\lambda \geq 535$ nm) for 15 minutes; (**C**) Schematic illustration of the particle analysis in ovo; (**D**) Organ distribution *in ovo* (n = 14), at 24 h post injection, determined by image analysis of fluorescence microscopy; (**E**) Representative fluorescence microscopy images for liver and kidney after injection of PCCPM-1 or PBS. In vitro data reported as mean ±

Standard Error of the Mean (SEM) and representative of 3 independent experiments. Two-way ANOVA(*): * $p < 0.05$, ** $p < 0.01$, *** $p < 0.001$, **** $p < 0.0001$.

Furthermore, free Ru-CPX-2 and PCCPM-2 only slightly induced additional toxicity that is significant relative to the irradiated control (Ru-CPX-2, $p < 0,01$; PCCPM-2, $p < 0,05$), whereby no more difference was observed among the free complex or the micellar formulation.

For further biologic evaluation, PCCPMs were covalently labeled with DBCO-sulforhodamine B by alkyne-azide click chemistry and investigated in the *in ovo* in the chorioallantoic membrane assay (CAM assay).[76] The CAM assay has been previously described as well suited model for the evaluation of nanoparticle toxicity and the study of circulation times, as well as clearance of nanoparticles from the organism.[77] As illustrated in Figure 6C, following intravascular administration of the particles, the circulation time was qualitatively analyzed by *in vivo* microscopy followed by surgical dissection and fluorescence microscopy of the fixated organ slices after the sacrifice of the embryo. Of the 19 eggs included in the study, 14 eggs finished the study according to protocol. Death of the embryo within the timeframe of observation as well as a lack of particle circulation due to paravasal injection were reasons for a dropout. Spherical photocleavable micelles showed a stable but decreasing circulation and were still detectable in circulation even 24 h post-injection (Figure S15). According to the histological analysis, the particles mainly sequestered in the tissue of liver and kidney (Figure 6D, E), and only minor accumulation was found in the heart, while hardly any particle-related fluorescence could be detected in the brain tissue slices (Figure S16). Of note, within the heart tissue the accumulation pattern was mostly disseminated and showed agglomerates predominantly in the vessels within the tissue, while in the brain tissue the fluorescent signal is mostly located within the vascular network. Since liver and kidney are the organs responsible for the excretion these are the typical sites where nanoparticles are deposited.[78,79]

Taken together, polypept(o)ides and ruthenium(II) complexes were successfully combined in photocleavable core cross-linked polymeric micelles. The cross-linking by the ruthenium(II) complexes provided colloidal stability, whereby the choice of the nitrile linker for complex conjugation showed a critical influence on the particle morphology. Light-induced cleavage and cytotoxicity was governed by the dense micellar core and the incorporated ruthenium(II) complex.

Conclusions

We demonstrate how polypept(o)ides and ruthenium(II) complexes can be combined for light-sensitive core cross-linked polymeric micelles. Block copolymers of pSar-*b*-pGlu that have been modified with flexible linkers containing aromatic nitrile moieties were self-assembled into spherical nanostructures and cross-linked by $[Ru(bpy)_2(H_2O)_2]$ $(PF_6)_2$ or $[Ru(biq)_2(H_2O)_2]$ $(PF_6)_2$ without affecting the overall size distribution (45 nm, PDI 0.11). The morphology was further tuned by changing to a shorter, less flexible, and less hydrophobic nitrile linker, whereby worm-like particles are observed in AFM and cryo-EM depending on the chain length of the modified pGlu block. According to the analysis by GPC in HFIP, the photocleavable core cross-linked polymeric micelles display colloidal stability and do not cause aggregation in human plasma as detected by DLS. Of note, after completed purification, rather low ruthenium complex contents of 4.3 to 4.8 wt.% have been determined by SN-ICP-MS yet seem sufficient for stabilization. By irradiation at the MLCT peak $[Ru(bpy)_2]^{2+}$ is completely cleaved within 5 minutes, whereas only insufficient light-induced solvolysis is observed for $[Ru(biq)_2]^{2+}$, which may be attributed to the low quantum yield and dense micellar core. Finally, the biologic evaluation underlines the potential of these functional metal- and polypept(o)ide-based nanomedicines, while future investigation for the application in photodynamic or photoactivated chemotherapy will focus on improving the cytotoxicity of the pro-drug complexes.

Author Contributions

All polymers and nanoparticles were synthesized, characterized, and evaluated by T.A.B., B.W. contributed multi-angle DLS and cryo-EM, F.K. and N.B. contributed SN-ICP-MS measurements. The ruthenium complexes were contributed by W.S. and X.Z. supervised by S.W. J.E. and N.W. performed *in vitro* and *in ovo* experiments guided by S.S. The manuscript was written by T.A.B., J.E., N.W., and M.B., the overall project was supervised by M.B.

Conflicts of interest

There are no conflicts to declare.

Acknowledgements

We would like to thank Andreas Braun (JGU Mainz) for the assembly of the high brightness LEDs. We thank Dr. Meike Schinnerer for DLS measurements in human plasma, and Dr. Ute Kolb and Dr. Frank Depoix for access to the TEM facility, and Holger Adam for maintenance of the AFM.

Notes and References

(1) Cabral, H.; Miyata, K.; Osada, K.; Kataoka, K. Block Copolymer Micelles in Nanomedicine Applications. *Chem. Rev.* **2018**, *118* (14), 6844–6892.

(2) Mi, P.; Miyata, K.; Kataoka, K.; Cabral, H. Clinical Translation of Self-Assembled Cancer Nanomedicines. *Adv. Ther.* **2021**, *4* (1), 2000159.

(3) Zhou, Q.; Zhang, L.; Yang, T. H.; Wu, H. Stimuli-Responsive Polymeric Micelles for Drug Delivery and Cancer Therapy. *Int. J. Nanomedicine* **2018**, *13*, 2921–2942.

(4) Rösler, A.; Vandermeulen, G. W. M.; Klok, H.-A. Advanced Drug Delivery Devices via Self-Assembly of Amphiphilic Block Copolymers. *Adv. Drug Deliv. Rev.* **2012**, *64*, 270–279.

(5) Talelli, M.; Barz, M.; Rijcken, C. J. F. F.; Kiessling, F.; Hennink, W. E.; Lammers, T. Core-Crosslinked Polymeric Micelles: Principles, Preparation, Biomedical Applications and Clinical Translation. *Nano Today* **2015**, *10* (1), 93–117.

(6) Owen, S. C.; Chan, D. P. Y.; Shoichet, M. S. Polymeric Micelle Stability. *Nano Today* **2012**, *7* (1), 53–65.

(7) Talelli, M.; Rijcken, C. J. F.; Hennink, W. E.; Lammers, T. Polymeric Micelles for Cancer Therapy: 3 C's to Enhance Efficacy. *Curr. Opin. Solid State Mater. Sci.* **2012**, *16* (6), 302–309.

(8) Barenholz, Y. Doxil® - The First FDA-Approved Nano-Drug: Lessons Learned. *J. Control. Release* **2012**, *160* (2), 117–134.

(9) Martinez, C. R.; Iverson, B. L. Rethinking the Term "Pi-Stacking." *Chem. Sci.* **2012**, *3* (7), 2191–2201.

(10) Liang, C.; Bai, X.; Qi, C.; Sun, Q.; Han, X.; Lan, T.; Zhang, H.; Zheng, X.; Liang, R.;

Jiao, J.; Zheng, Z.; Fang, J.; Lei, P.; Wang, Y.; Möckel, D.; Metselaar, J. M.; Storm, G.; Hennink, W. E.; Kiessling, F.; Wei, H.; Lammers, T.; Shi, Y.; Wei, B. Π Electron-Stabilized Polymeric Micelles Potentiate Docetaxel Therapy in Advanced-Stage Gastrointestinal Cancer. *Biomaterials* **2021**, *266* (September 2020), 10.

(11) Shi, Y.; Van Steenbergen, M. J.; Teunissen, E. A.; Novo, L.; Gradmann, S.; Baldus, M.; Van Nostrum, C. F.; Hennink, W. E. Π-Π Stacking Increases the Stability and Loading Capacity of Thermosensitive Polymeric Micelles for Chemotherapeutic Drugs. *Biomacromolecules* **2013**, *14* (6), 1826–1837.

(12) Lin, M.; Dai, Y.; Xia, F.; Zhang, X. Advances in Non-Covalent Crosslinked Polymer Micelles for Biomedical Applications. *Mater. Sci. Eng. C* **2021**, *119* (September 2020), 111626.

(13) Deng, C.; Zhang, Q.; Guo, J.; Zhao, X.; Zhong, Z. Robust and Smart Polypeptide-Based Nanomedicines for Targeted Tumor Therapy. *Adv. Drug Deliv. Rev.* **2020**, *160*, 199–211.

(14) Atrafi, F.; Dumez, H.; Mathijssen, R. H. J.; Menke van der Houven van Oordt, C. W.; Rijcken, C. J. F.; Hanssen, R.; Eskens, F. A. L. M.; Schöffski, P. A Phase I Dose-Escalation and Pharmacokinetic Study of a Micellar Nanoparticle with Entrapped Docetaxel (CPC634) in Patients with Advanced Solid Tumours. *J. Control. Release* **2020**, *325* (March), 191–197.

(15) Rijcken, C. J.; Snel, C. J.; Schiffelers, R. M.; van Nostrum, C. F.; Hennink, W. E. Hydrolysable Core-Crosslinked Thermosensitive Polymeric Micelles: Synthesis, Characterisation and in Vivo Studies. *Biomaterials* **2007**, *28* (36), 5581–5593.

(16) Atrafi, F.; van Eerden, R. A. G.; van Hylckama Vlieg, M. A. M.; Oomen-de Hoop, E.; de Bruijn, P.; Lolkema, M. P.; Moelker, A.; Rijcken, C. J.; Hanssen, R.; Sparreboom, A.; Eskens, F. A. L. M.; Mathijssen, R. H. J.; Koolen, S. L. W. Intratumoral Comparison of Nanoparticle Entrapped Docetaxel (CPC634) with Conventional Docetaxel in Patients with Solid Tumors. *Clin. Cancer Res.* **2020**, *26* (14), 3537–3545.

(17) Van Eerden, R. A. G.; Mathijssen, R. H. J.; Koolen, S. L. W. Recent Clinical Developments of Nanomediated Drug Delivery Systems of Taxanes for the Treatment of Cancer. *Int. J. Nanomedicine* **2020**, *15*, 8151–8166.

(18) Nishiyama, N.; Okazaki, S.; Cabral, H.; Miyamoto, M.; Kato, Y.; Sugiyama, Y.; Nishio, K.; Matsumura, Y.; Kataoka, K. Novel Cisplatin-Incorporated Polymeric Micelles Can Eradicate Solid Tumors in Mice. *Cancer Res.* **2003**, *63* (24), 8977–8983.

(19) Plummer, R.; Wilson, R. H.; Calvert, H.; Boddy, A. V.; Griffin, M.; Sludden, J.; Tilby, M. J.; Eatock, M.; Pearson, D. G.; Ottley, C. J.; Matsumura, Y.; Kataoka, K.; Nishiya, T. A Phase i Clinical Study of Cisplatin-Incorporated Polymeric Micelles (NC-6004) in Patients with Solid Tumours. *Br. J. Cancer* **2011**, *104* (4), 593–598.

(20) Mochida, Y.; Cabral, H.; Miura, Y.; Albertini, F.; Fukushima, S.; Osada, K.; Nishiyama, N.; Kataoka, K. Bundled Assembly of Helical Nanostructures in Polymeric Micelles Loaded with Platinum Drugs Enhancing Therapeutic Efficiency against Pancreatic Tumor. *ACS Nano* **2014**, *8* (7), 6724–6738.

(21) Bonnet, S. Why Develop Photoactivated Chemotherapy? *Dalt. Trans.* **2018**, *47* (31), 10330–10343.

(22) Farrer, N. J.; Salassa, L.; Sadler, P. J. Photoactivated Chemotherapy (PACT): The Potential of Excited-State d-Block Metals in Medicine. *Dalt. Trans.* **2009**, No. 48,

10690.

(23) Williams, R. L.; Toft, H. N.; Winkel, B.; Brewer, K. J. Synthesis, Characterization, and DNA Binding Properties of a Series of Ru, Pt Mixed-Metal Complexes. *Inorg. Chem.* **2003**, *42* (14), 4394–4400.

(24) Li, W.; Jiang, G. Bin; Yao, J. H.; Wang, X. Z.; Wang, J.; Han, B. J.; Xie, Y. Y.; Lin, G. J.; Huang, H. L.; Liu, Y. J. Ruthenium(II) Complexes: DNA-Binding, Cytotoxicity, Apoptosis, Cellular Localization, Cell Cycle Arrest, Reactive Oxygen Species, Mitochondrial Membrane Potential and Western Blot Analysis. *J. Photochem. Photobiol. B Biol.* **2014**, *140*, 94–104.

(25) Villemin, E.; Ong, Y. C.; Thomas, C. M.; Gasser, G. Polymer Encapsulation of Ruthenium Complexes for Biological and Medicinal Applications. *Nat. Rev. Chem.* **2019**, *3* (4), 261–282.

(26) Singh, T. N.; Turro, C. Photoinitiated DNA Binding by Cis-[Ru(Bpy)2(NH3)2]2+. *Inorg. Chem.* **2004**, *43* (23), 7260–7262.

(27) Knoll, J. D.; Albani, B. A.; Turro, C. New Ru(II) Complexes for Dual Photoreactivity: Ligand Exchange and 1 O 2 Generation. *Acc. Chem. Res.* **2015**, *48* (8), 2280–2287.

(28) Sun, W.; Wen, Y.; Thiramanas, R.; Chen, M.; Han, J.; Gong, N.; Wagner, M.; Jiang, S.; Meijer, M. S.; Bonnet, S.; Butt, H.; Mailänder, V.; Liang, X.; Wu, S. Red-Light-Controlled Release of Drug-Ru Complex Conjugates from Metallopolymer Micelles for Phototherapy in Hypoxic Tumor Environments. *Adv. Funct. Mater.* **2018**, *28* (39), 1804227.

(29) Sun, W.; Li, S.; Häupler, B.; Liu, J.; Jin, S.; Steffen, W.; Schubert, U. S.; Butt, H.-J. J.; Liang, X.-J. J.; Wu, S. An Amphiphilic Ruthenium Polymetallodrug for Combined Photodynamic Therapy and Photochemotherapy In Vivo. *Adv. Mater.* **2017**, *29* (6), 1603702.

(30) Sun, W.; Parowatkin, M.; Steffen, W.; Butt, H. J.; Mailänder, V.; Wu, S. Ruthenium-Containing Block Copolymer Assemblies: Red-Light-Responsive Metallopolymers with Tunable Nanostructures for Enhanced Cellular Uptake and Anticancer Phototherapy. *Adv. Healthc. Mater.* **2016**, *5* (4), 467–473.

(31) Zeng, X.; Wang, Y.; Han, J.; Sun, W.; Butt, H. J.; Liang, X. J.; Wu, S. Fighting against Drug-Resistant Tumors Using a Dual-Responsive Pt(IV)/Ru(II) Bimetallic Polymer. *Adv. Mater.* **2020**, *32* (43), 1–9.

(32) Birke, A.; Ling, J.; Barz, M. Polysarcosine-Containing Copolymers: Synthesis, Characterization, Self-Assembly, and Applications. *Prog. Polym. Sci.* **2018**, *81*, 163–208.

(33) Klinker, K.; Barz, M. Polypept(o)Ides: Hybrid Systems Based on Polypeptides and Polypeptoids. *Macromol. Rapid Commun.* **2015**, *36* (22), 1943–1957.

(34) Birke, A.; Huesmann, D.; Kelsch, A.; Weilbächer, M.; Xie, J.; Bros, M.; Bopp, T.; Becker, C.; Landfester, K.; Barz, M. Polypeptoid- Block -Polypeptide Copolymers: Synthesis, Characterization, and Application of Amphiphilic Block Copolypept(o)ides in Drug Formulations and Miniemulsion Techniques. *Biomacromolecules* **2014**, *15* (2), 548–557.

(35) Vayaboury, W.; Giani, O.; Cottet, H.; Deratani, A.; Schué, F. Living Polymerization of α-Amino Acid N-Carboxyanhydrides (NCA) upon Decreasing the Reaction Temperature. *Macromol. Rapid Commun.* **2004**, *25* (13), 1221–1224.

(36) Aliferis, T.; Iatrou, H.; Hadjichristidis, N. Living Polypeptides. *Biomacromolecules* **2004**, *5* (5), 1653–1656.

(37) Fetsch, C.; Grossmann, A.; Holz, L.; Nawroth, J. F.; Luxenhofer, R. Polypeptoids from N -Substituted Glycine N -Carboxyanhydrides: Hydrophilic, Hydrophobic, and Amphiphilic Polymers with Poisson Distribution. *Macromolecules* **2011**, *44* (17), 6746–6758.

(38) Alberg, I.; Kramer, S.; Schinnerer, M.; Hu, Q.; Seidl, C.; Leps, C.; Drude, N.; Möckel, D.; Rijcken, C.; Lammers, T.; Diken, M.; Maskos, M.; Morsbach, S.; Landfester, K.; Tenzer, S.; Barz, M.; Zentel, R. Polymeric Nanoparticles with Neglectable Protein Corona. *Small* **2020**, *16* (18), 1907574.

(39) Weber, B.; Birke, A.; Fischer, K.; Schmidt, M.; Barz, M. Solution Properties of Polysarcosine: From Absolute and Relative Molar Mass Determinations to Complement Activation. *Macromolecules* **2018**, *51* (7), 2653–2661.

(40) Lau, K. H. A.; Ren, C.; Sileika, T. S.; Park, S. H.; Szleifer, I.; Messersmith, P. B. Surface-Grafted Polysarcosine as a Peptoid Antifouling Polymer Brush. *Langmuir* **2012**, *28* (46), 16099–16107.

(41) Deming, T. J. Synthesis of Side-Chain Modified Polypeptides. *Chem. Rev.* **2016**, *116* (3), 786–808.

(42) Klinker, K.; Schäfer, O.; Huesmann, D.; Bauer, T.; Capelôa, L.; Braun, L.; Stergiou, N.; Schinnerer, M.; Dirisala, A.; Miyata, K.; Osada, K.; Cabral, H.; Kataoka, K.; Barz, M. Secondary-Structure-Driven Self-Assembly of Reactive Polypept(o)Ides: Controlling Size, Shape, and Function of Core Cross-Linked Nanostructures. *Angew. Chemie Int. Ed.* **2017**, *56* (32), 9608–9613.

(43) Heller, P.; Zhou, J.; Weber, B.; Hobernik, D.; Bros, M.; Schmid, F.; Barz, M. The Influence of Block Ionomer Microstructure on Polyplex Properties: Can Simulations Help to Understand Differences in Transfection Efficiency? *Small* **2017**, *13* (17), 1603694.

(44) Nogueira, S. S.; Schlegel, A.; Maxeiner, K.; Weber, B.; Barz, M.; Schroer, M. A.; Blanchet, C. E.; Svergun, D. I.; Ramishetti, S.; Peer, D.; Langguth, P.; Sahin, U.; Haas, H. Polysarcosine-Functionalized Lipid Nanoparticles for Therapeutic MRNA Delivery. *ACS Appl. Nano Mater.* **2020**, *3* (11), 10634–10645.

(45) Son, K.; Ueda, M.; Taguchi, K.; Maruyama, T.; Takeoka, S.; Ito, Y. Evasion of the Accelerated Blood Clearance Phenomenon by Polysarcosine Coating of Liposomes. *J. Control. Release* **2020**, *322* (March), 209–216.

(46) Barz, M.; Luxenhofer, R.; Zentel, R.; Vicent, M. J. Overcoming the PEG-Addiction: Well-Defined Alternatives to PEG, from Structure–Property Relationships to Better Defined Therapeutics. *Polym. Chem.* **2011**, *2* (9), 1900–1918.

(47) Rausch, K.; Reuter, A.; Fischer, K.; Schmidt, M. Evaluation of Nanoparticle Aggregation in Human Blood Serum. *Biomacromolecules* **2010**, *11* (11), 2836–2839.

(48) Theis, S.; Iturmendi, A.; Gorsche, C.; Orthofer, M.; Lunzer, M.; Baudis, S.; Ovsianikov, A.; Liska, R.; Monkowius, U.; Teasdale, I. Metallo-Supramolecular Gels That Are Photocleavable with Visible and Near-Infrared Irradiation. *Angew. Chemie - Int. Ed.* **2017**, *56* (50), 15857–15860.

(49) Holm, R.; Klinker, K.; Weber, B.; Barz, M. Synthesis of Amphiphilic Block Copolypept(o)Ides by Bifunctional Initiators: Making PeptoMicelles Redox

Sensitive. *Macromol. Rapid Commun.* **2015**, *36* (23), 2083–2091.

(50) Steinborn, B.; Hirschle, P.; Höhn, M.; Bauer, T.; Barz, M.; Wuttke, S.; Wagner, E.; Lächelt, U. Core-Shell Functionalized Zirconium-Pemetrexed Coordination Nanoparticles as Carriers with a High Drug Content. *Adv. Ther.* **2019**, *2* (11), 1900120.

(51) Ernst, B. P.; Wiesmann, N.; Gieringer, R.; Eckrich, J.; Brieger, J. HSP27 Regulates Viability and Migration of Cancer Cell Lines Following Irradiation. *J. Proteomics* **2020**, *226* (March), 103886.

(52) Schäfer, O.; Klinker, K.; Braun, L.; Huesmann, D.; Schultze, J.; Koynov, K.; Barz, M. Combining Orthogonal Reactive Groups in Block Copolymers for Functional Nanoparticle Synthesis in a Single Step. *ACS Macro Lett.* **2017**, *6* (10), 1140–1145.

(53) Conejos-Sánchez, I.; Duro-Castano, A.; Birke, A.; Barz, M.; Vicent, M. J. A Controlled and Versatile NCA Polymerization Method for the Synthesis of Polypeptides. *Polym. Chem.* **2013**, *4* (11), 3182.

(54) Gangloff, N.; Fetsch, C.; Luxenhofer, R. Polypeptoids by Living Ring-Opening Polymerization of N-Substituted N-Carboxyanhydrides from Solid Supports. *Macromol. Rapid Commun.* **2013**, *34* (12), 997–1001.

(55) Durham, B.; Wilson, S. R.; Hodgson, D. J.; Meyer, T. J. Cis-Trans Photoisomerization in Ru(Bpy)2(OH2)22+. Crystal Structure of Trans-[Ru(Bpy)2(OH2)(OH)](ClO4)2. *J. Am. Chem. Soc.* **1980**, *102* (2), 600–607.

(56) Kobayashi, K.; Ohtsu, H.; Nozaki, K.; Kitagawa, S.; Tanaka, K. Photochemical Properties and Reactivity of a Ru Compound Containing an NAD/NADH-Functionalized 1,10-Phenanthroline Ligand. *Inorg. Chem.* **2016**, *55* (5), 2076–2084.

(57) Lammers, T. SMART Drug Delivery Systems: Back to the Future vs. Clinical Reality. *Int. J. Pharm.* **2013**, *454* (1), 527–529.

(58) Mitragotri, S.; Lammers, T.; Bae, Y. H.; Schwendeman, S.; De Smedt, S.; Leroux, J. C.; Peer, D.; Kwon, I. C.; Harashima, H.; Kikuchi, A.; Oh, Y. K.; Torchilin, V.; Hennink, W.; Hanes, J.; Park, K. Drug Delivery Research for the Future: Expanding the Nano Horizons and Beyond. *J. Control. Release* **2017**, *246*, 183–184.

(59) Soetaert, F.; Korangath, P.; Serantes, D.; Fiering, S.; Ivkov, R. Cancer Therapy with Iron Oxide Nanoparticles: Agents of Thermal and Immune Therapies. *Adv. Drug Deliv. Rev.* **2020**, *163–164*, 65–83.

(60) Bhattacharjee, S. DLS and Zeta Potential - What They Are and What They Are Not? *J. Control. Release* **2016**, *235*, 337–351.

(61) Fischer, K.; Schmidt, M. Pitfalls and Novel Applications of Particle Sizing by Dynamic Light Scattering. *Biomaterials* **2016**, *98*, 79–91.

(62) Franken, L. E.; Boekema, E. J.; Stuart, M. C. A. Transmission Electron Microscopy as a Tool for the Characterization of Soft Materials: Application and Interpretation. *Adv. Sci.* **2017**, *4* (5), 1–9.

(63) Lecommandoux, S.; Achard, M. F.; Langenwalter, J. F.; Klok, H. A. Self-Assembly of Rod-Coil Diblock Oligomers Based on α-Helical Peptides. *Macromolecules* **2001**, *34* (26), 9100–9111.

(64) Bonduelle, C. Secondary Structures of Synthetic Polypeptide Polymers. *Polym. Chem.* **2018**, *9* (13), 1517–1529.

(65) Palmer, L. C.; Stupp, S. I. Molecular Self-Assembly into One-Dimensional

Nanostructures. *Acc. Chem. Res.* **2008**, *41* (12), 1674–1684.

(66) Bauer, T. A.; Imschweiler, J.; Muhl, C.; Weber, B.; Barz, M. Secondary Structure-Driven Self-Assembly of Thiol-Reactive Polypept(o)Ides. *Biomacromolecules* **2021**, *22* (5), 2171–2180.

(67) Garner, R. N.; Gallucci, J. C.; Dunbar, K. R.; Turro, C. [Ru(Bpy) 2 (5-Cyanouracil) 2] 2+ as a Potential Light-Activated Dual-Action Therapeutic Agent. *Inorg. Chem.* **2011**, *50* (19), 9213–9215.

(68) Garner, R. N.; Joyce, L. E.; Turro, C. Effect of Electronic Structure on the Photoinduced Ligand Exchange of Ru(II) Polypyridine Complexes. *Inorg. Chem.* **2011**, *50* (10), 4384–4391.

(69) Albani, B. A.; Durr, C. B.; Turro, C. Selective Photoinduced Ligand Exchange in a New Tris-Heteroleptic Ru (II) Complex Selective Photoinduced Ligand Exchange in a New Tris-Heteroleptic Ru (II) Complex. *J. Phys. Chem. A* **2013**, *117* (Ii), 13885–13892.

(70) Liu, Y.; Turner, D. B.; Singh, T. N.; Angeles-Boza, A. M.; Chouai, A.; Dunbar, K. R.; Turro, C. Ultrafast Ligand Exchange: Detection of a Pentacoordinate Ru(II) Intermediate and Product Formation. *J. Am. Chem. Soc.* **2009**, *131* (1), 26–27.

(71) Zeng, L.; Gupta, P.; Chen, Y.; Wang, E.; Ji, L.; Chao, H.; Chen, Z. S. The Development of Anticancer Ruthenium(II) Complexes: From Single Molecule Compounds to Nanomaterials. *Chem. Soc. Rev.* **2017**, *46* (19), 5771–5804.

(72) Nováková, O.; Kašpárková, J.; Vrána, O.; van Vliet, P. M.; Reedijk, J.; Brabec, V. Correlation between Cytotoxicity and DNA Binding of Polypyridyl Ruthenium Complexes. *Biochemistry* **1995**, *34* (38), 12369–12378.

(73) Vázquez, M.; Martínez, M. Kinetico-Mechanistic Studies on the Substitution Reactivity on the {Ru II (Bpy) 2 } Core with Nucleosides and Nucleotides at Physiological PH. *Inorg. Chem.* **2016**, *55* (13), 6731–6738.

(74) Cuello-Garibo, J.-A.; Meijer, M. S.; Bonnet, S. To Cage or to Be Caged? The Cytotoxic Species in Ruthenium-Based Photoactivated Chemotherapy Is Not Always the Metal. *Chem. Commun.* **2017**, *53* (50), 6768–6771.

(75) Azar, D.; Audi, H.; Farhat, S.; El Sibai, M.; Abi-Habib, R.; Khnayzer, R. S. Phototoxicity of Strained Ru(II) Complexes: Is It the Metal Complex or the Dissociating Ligand? *Dalt. Trans.* **2017**, *46* (35), 11529–11532.

(76) Buhr, C. R.; Wiesmann, N.; Tanner, R. C.; Brieger, J.; Eckrich, J. The Chorioallantoic Membrane Assay in Nanotoxicological Research—an Alternative for in Vivo Experimentation. *Nanomaterials* **2020**, *10* (12), 1–16.

(77) Ribatti, D. The Chick Embryo Chorioallantoic Membrane (CAM). A Multifaceted Experimental Model. *Mech. Dev.* **2016**, *141*, 70–77.

(78) Poon, W.; Heinmiller, A.; Zhang, X.; Nadeau, J. L. Determination of Biodistribution of Ultrasmall, near-Infrared Emitting Gold Nanoparticles by Photoacoustic and Fluorescence Imaging. *J. Biomed. Opt.* **2015**, *20* (6), 066007.

(79) Buhr, C. R.; Eckrich, J.; Kluenker, M.; Bruns, K.; Wiesmann, N.; Tremel, W.; Brieger, J. Determination of the LD 50 with the Chick Embryo Chorioallantoic Membrane (CAM) Assay as a Promising Alternative in Nanotoxicological Evaluation. *Nanotoxicology* **2021**, 1–16.

Supporting Information

Results and Discussion

Polymer Synthesis

Table S1. Analytical results of the polymer synthesis of **P1** to **P9**.

polymer	*M/I (calc.)*	X_n (pGlu)[a]	X_n (pSar)[a]	M_n[b] / kDa	M_w[b] / kDa	$Đ$[b]	CN-grafting
P1, pGlu(O*t*Bu)$_{36}$	30	36	-	19.7	22.9	1.16	-
P2, pGlu(O*t*Bu)$_{36}$-*b*-Sar$_{171}$	160	36	171	44.0	52.9	1.20	-
P3, pGlu(OH)$_{36}$-*b*-Sar$_{171}$	-	36	171	37.9	59.1	1.56	-
P4, pGlu(Mod)$_{36}$-*b*-Sar$_{171}$	-	36	171	53.1	74.8	1.41	52%
P5, *N*-Boc-pSar$_{140}$	200	-	140	-	-	-	-
P6, pSar$_{140}$	-	-	140	28.7	34.5	1.20	-
P7A, pSar$_{140}$-*b*-pGlu(O*t*Bu)$_{20}$	20	19	140	30.0	39.3	1.31	-
P7B, pSar$_{140}$-*b*-pGlu(O*t*Bu)$_{15}$	15	14	140	30.3	40.7	1.34	-
P8A, pSar$_{140}$-*b*-pGlu(OH)$_{20}$	-	19	140	28.2	35.6	1.26	-
P8B, pSar$_{140}$-*b*-pGlu(OH)$_{15}$	-	14	140	30.9	54.1	1.75	-
P9A, pSar$_{140}$-*b*-pGlu(Mod)$_{20}$	-	19	140	71.3	113.2	1.58	65%
P9B, pSar$_{140}$-*b*-pGlu(Mod)$_{15}$	-	14	140	47.9	61.5	1.28	100%

[a] determined by ^{1}H NMR, [b] determined by HFIP-GPC with pSar standards, [c] determined by HFIP-GPC with PMMA standards.

HFIP-GPC Analysis

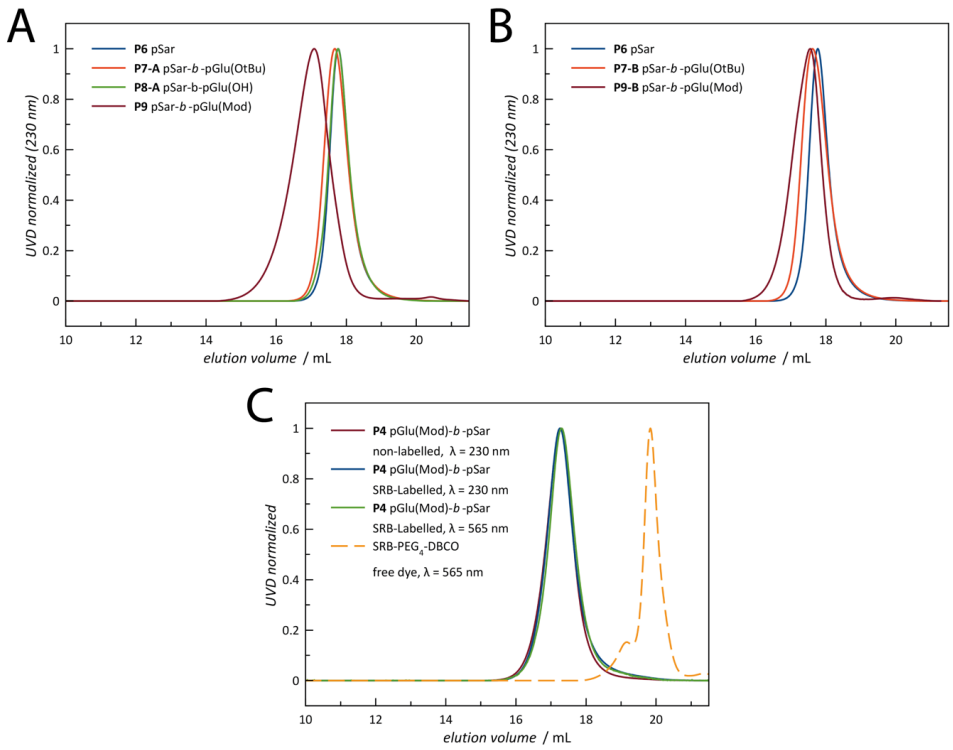

Figure S1. Analytical HFIP-GPC. (**A**) Polymers P6 to P9-A, (**B**) Polymers P6 to P9-B, (**C**) Labelling of P4 with Sulforhodamine-B, whereby no free unconjugated dye is detectable.

FT-IR Spectroscopy

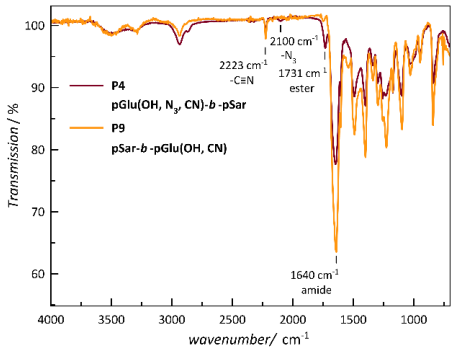

Figure S2. Comparison of cyano-modified polymers P4 (dark red) and P9-A (orange) by FT-IR spectroscopy. As expected, the ester bond is not visible in P9-A, but only in P4.

Photocleavable Core Cross-Linked Polymeric Micelles (PCCPMs)

Images

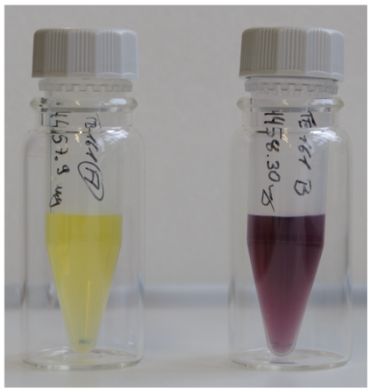

Figure S3. Images of PCCPMs after completed purification by spin-filtration. PCCPM-1 (left) and PCCPM-2 (right).

Multi-Angle Dynamic Light Scattering in Human Plasma

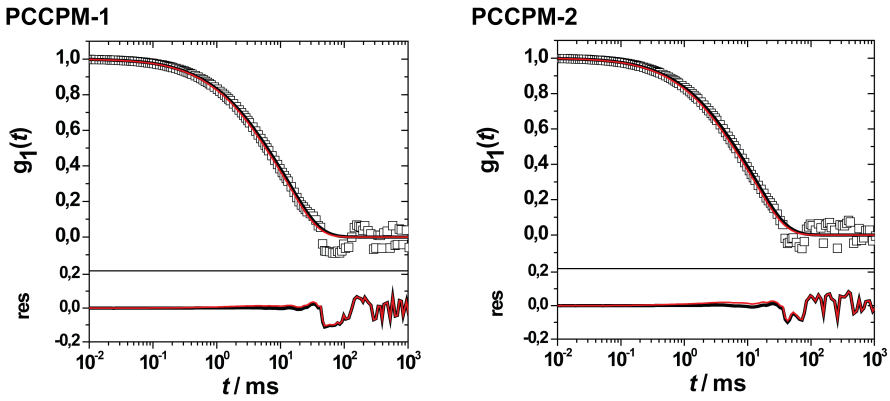

Figure S4. Multi-Angle Dynamic Light Scattering of PCCPM-1 (left) and PCCPM-2 (right) in human plasma.[1] Autocorrelation function $g_1(t)$ for an exemplary scattering angle of 30° for fits with (red) and without (black line) aggregate term (upper graph), and the residuals of fits w/o aggregate and correlation function (lower graph).

Extended TEM Analysis

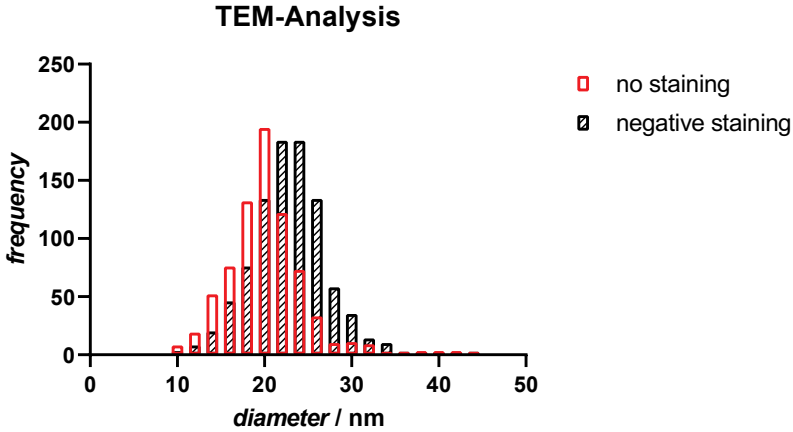

Figure S5. Particle analysis by TEM for PCCPM-2. (red) without staining; average particle diameter of 20.2 ± 4.5 nm, PDI 0.050. (black) negatively stained with uranyl acetate; average particle diameter of 22.8 ± 4.3 nm, PDI 0.034. Objects smaller than 10 nm diameter were excluded for statistics.

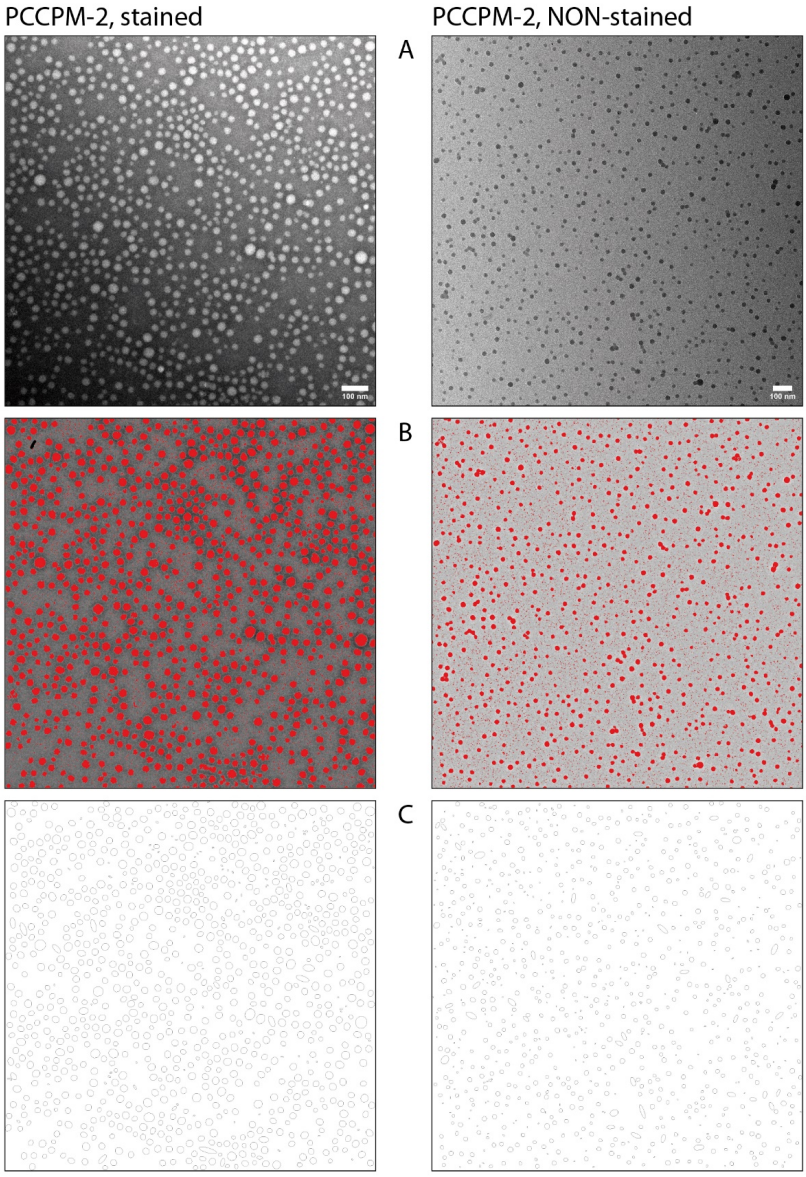

Figure S6. Exemplified particle counting for non-stained (left) and negatively stained samples (right) using ImageJ 1.52h.(**A**) parent TEM image, (**B**) derived threshold image, (**C**) area analysis for given threshold objects. Assuming spherical shape, diameters were calculated for each object.

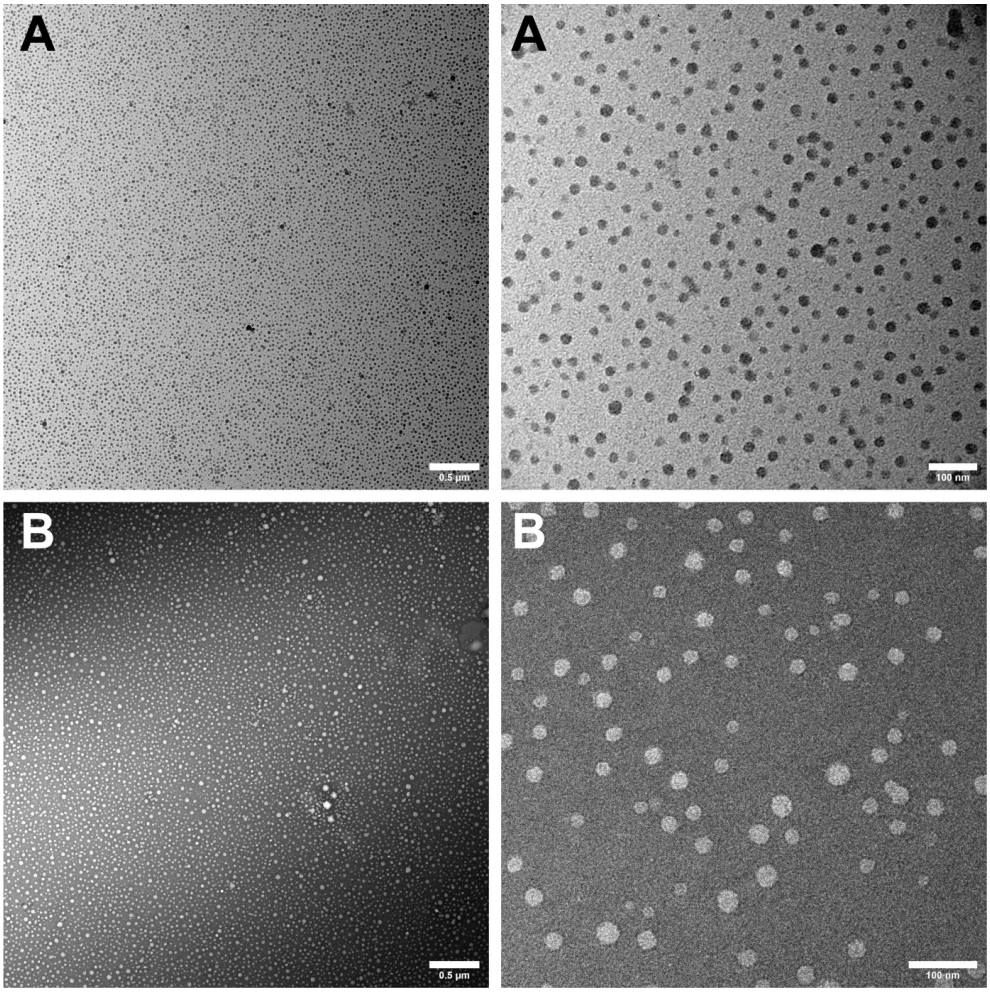

Figure S7. TEM Analysis of PCCPM-1. (**A**) without staining, (**B**) negative staining.

Worm-like Photocleavable Core Cross-Linked Polymeric Micelles (w-PCCPM)

Multi-Angle Dynamic Light Scattering of Worm-Like PCCPMs

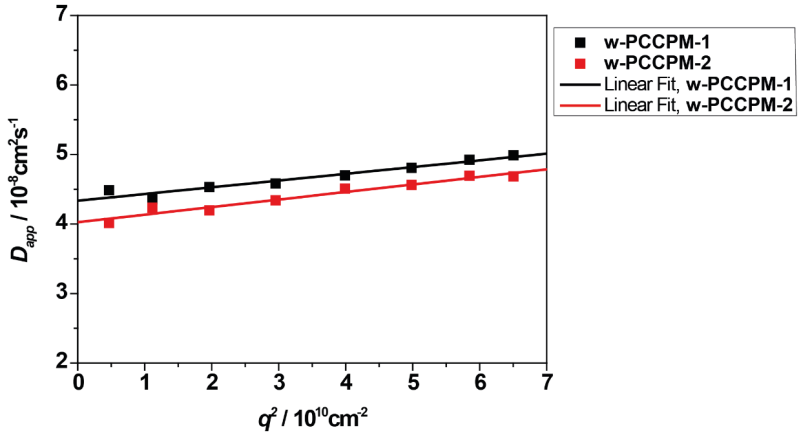

Figure S8. Multi-angle dynamic light scattering of worm-like PCCPMs in PBS prepared from **P9-A**.

AFM Analysis of Worm-Like PCCPMs

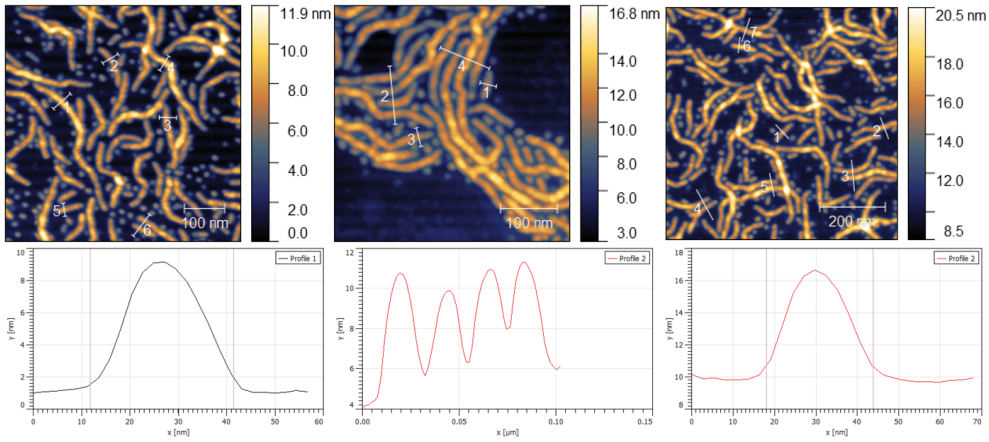

Figure S9. AFM image analysis of w-PCCPM-1. AFM images with indicated profiles (lower) and exemplary apparent height profiles.

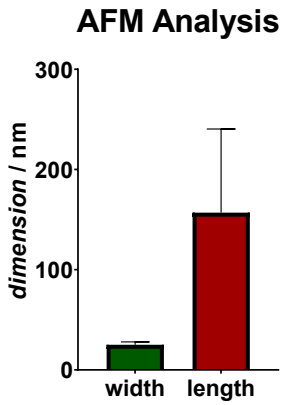

Figure S10. AFM image analysis of w-PCCPM-1. Average rod width 25 ± 3 nm (N = 27); Average rod length 157 ± 83 nm (N = 90).

Block Length Variations for Spherical PCCPMs

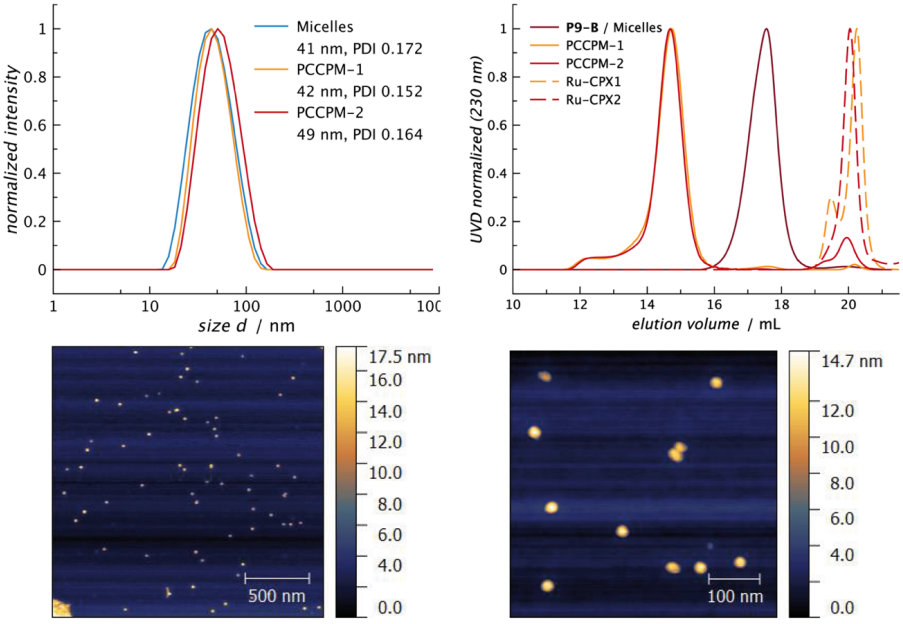

Figure S11. Spherical PCCPMs from amide-modified $pSar_{140}$-*b*-$pGlu_{15}$ block copolymer. Only slight bimodal GPC-trace. PCCPM-2 shows large amounts of non-covalent Ru-CPX-encapsulation, well corresponding with higher drug contents (11.84 wt.%).

Table S2. Characterization of spherical PCCPMs from pSar$_{140}$-*b*-pGlu(Mod)$_{15}$ (**P9-B**).

particle	Ru-CPX	D_h / nm[a]	*PDI*[a]	D_h / nm[b]	*Ru-CPX-content* / wt.%
Micelles/P9-B	-	41	0.172	-	-
PCCPM-1/P9-B	$[Ru(bpy)_2]^{2+}$	42	0.152	63	3.19 ± 0.25
PCCPM-2/P9-B	$[Ru(biq)_2]^{2+}$	49	0.164	71	11.84 ± 0.93

[a] determined by single-angle dynamic light scattering at an angle of 173°, [b] determined by multi-angle light scattering, [c] determined by ICP-MS.

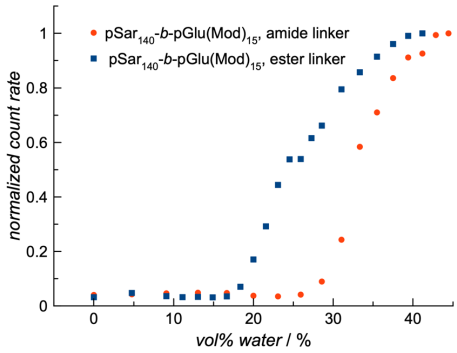

Figure S12. DLS count rate analysis accounts for aggregation of modified pSar$_{140}$-*b*-pGlu(Mod)$_{15}$ copolymers. Copolymers were dissolved in DMSO (5 g·L^{-1}) and water was added sequentially.

Photocleavage

UV-Vis Spectroscopy

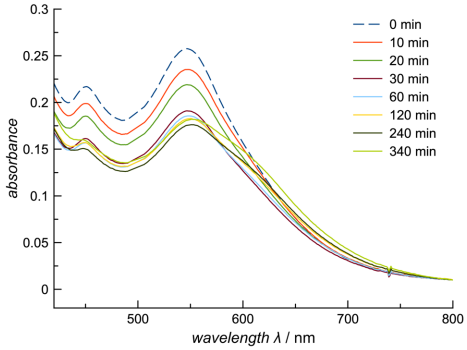

Figure S13. Photocleavage of PCCPM-2 with a red-orange LED (620 nm).

Biological Evaluation

In vitro Studies

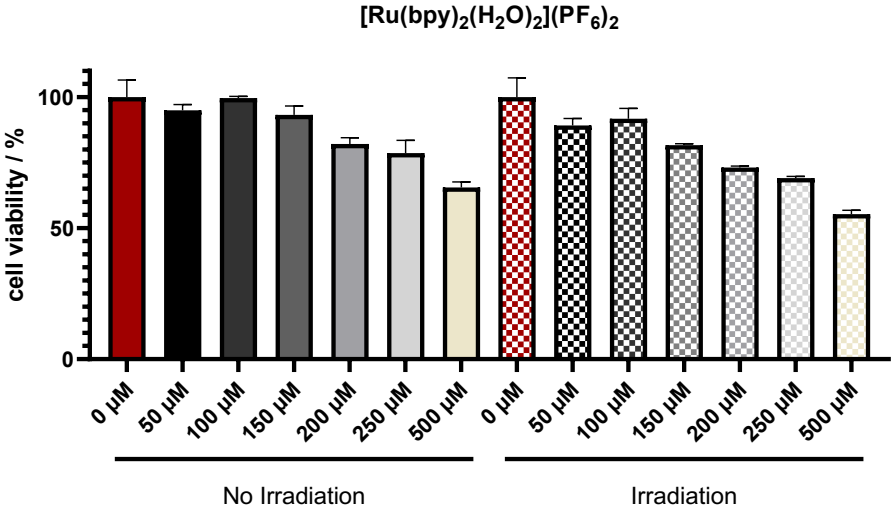

Figure S14. Viability of HuH-7 cells after incubation with Ru-CPX-1 for 24 h with or without irradiation relative to untreated control (0 µM), as analyzed by Alamar Blue Assay.

In ovo Studies

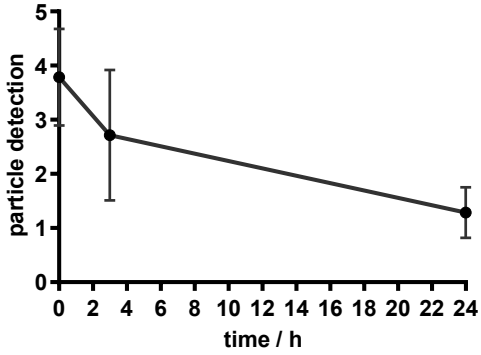

Figure S15. Analysis of intravascular circulation. After intravascular application of the sulforhodamine B labeled nanoparticles, in vivo fluorescent microscopy was performed. After blinding, video sequences were investigated repetitively three times. As the intensity of particles in the vascular system did not allow a sufficient quantitative analysis the following numerical analogue scale was applied: 5 = intravascular nanoparticles can be detected ubiquitously; 4 = intravascular nanoparticles can be detected predominantly; 3 = intravascular nanoparticles can be detected occasionally; 2 = nanoparticles can be detected; 1 = no nanoparticles can be detected. Data shown as Mean + Error.

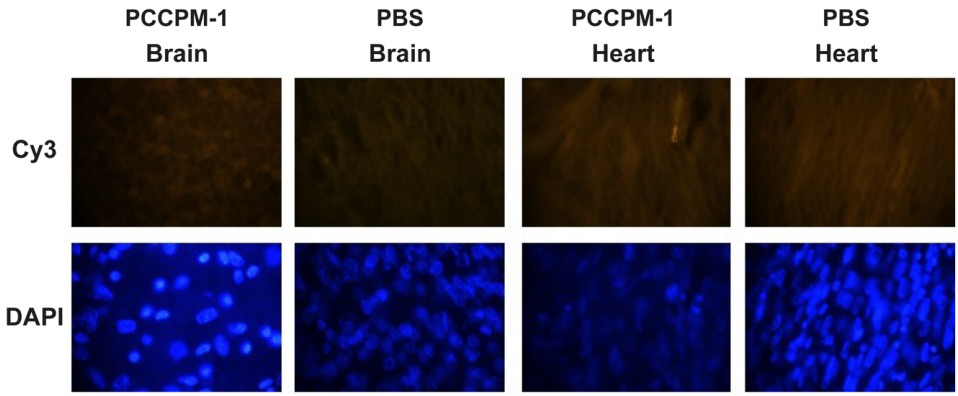

Figure S16. Representative fluorescence microscopy images of brain and heart tissue taken with the Cy3 and DAPI filter after application of sulforhodamine B labeled PCCPM or control (PBS).

References for Supporting Information

(1) Rausch, K.; Reuter, A.; Fischer, K.; Schmidt, M. Evaluation of Nanoparticle Aggregation in Human Blood Serum. *Biomacromolecules* **2010**, *11* (11), 2836–2839.

Appendix

^{1}H NMR Spectroscopy

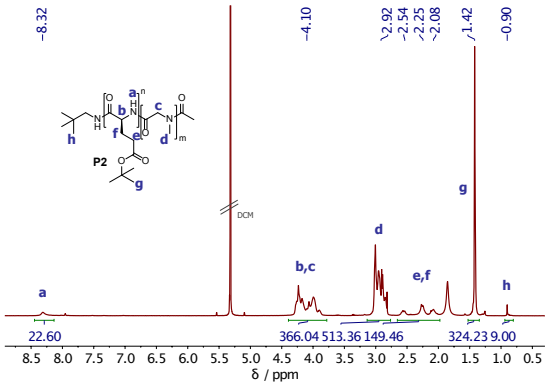

Figure S17. ^{1}H NMR spectrum of **P2** (pGlu(O*t*Bu)$_{36}$-*b*-pSar$_{171}$) in CD_2Cl_2.

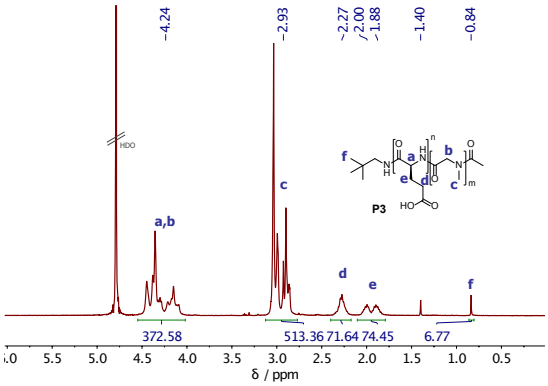

Figure S18. ^{1}H NMR spectrum of **P3** (pGlu(OH)$_{36}$-*b*-pSar$_{171}$) in D_2O.

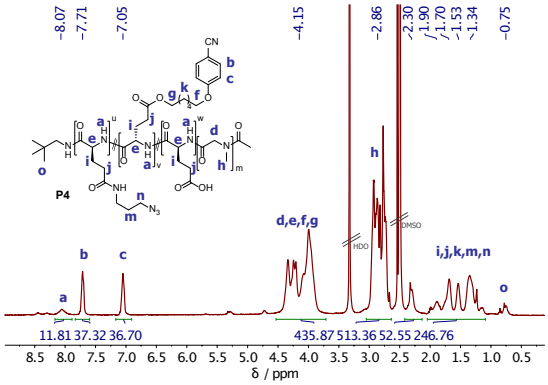

Figure S19. ^{1}H NMR spectrum of **P4** (pGlu(Mod)$_{36}$-*b*-pSar$_{171}$) in DMSO-*d*$_6$.

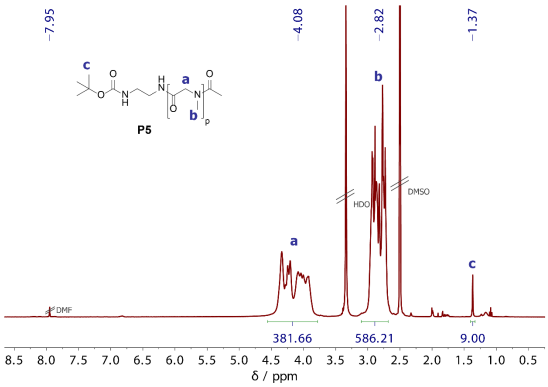

Figure S20. ^{1}H NMR spectrum of **P5** (*N*-Boc-pSar$_{140}$) in DMSO-*d*$_6$.

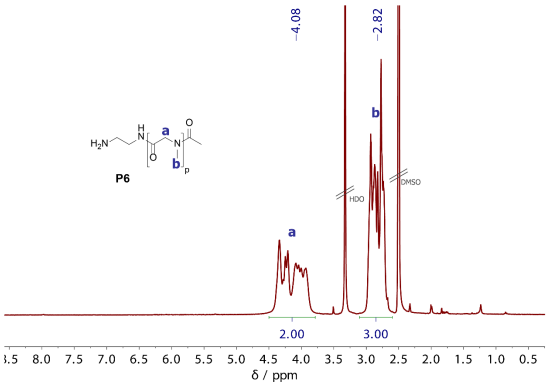

Figure S21. ^{1}H NMR spectrum of **P6** (pSar$_{140}$) in DMSO-*d*$_6$.

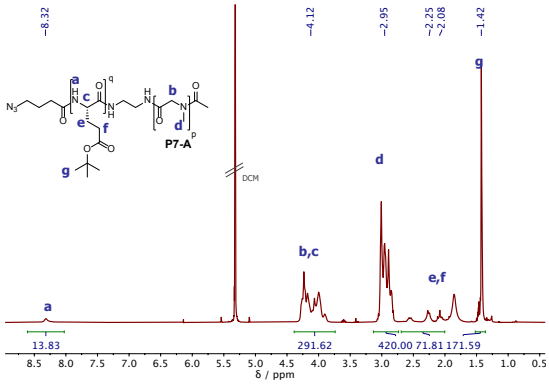

Figure S22. ^{1}H NMR spectrum of **P7-A** (pSar$_{140}$-*b*-pGlu(O*t*Bu)$_{20}$) in CD_2Cl_2.

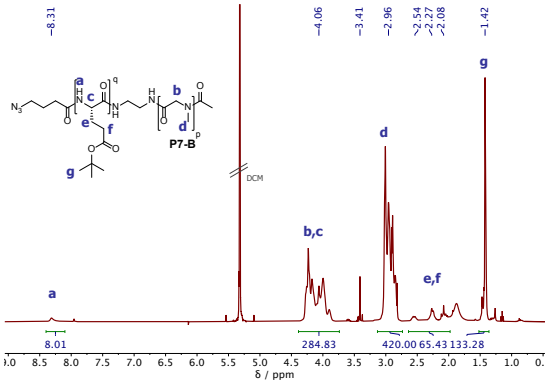

Figure S23. ^{1}H NMR spectrum of **P7-B** (pSar$_{140}$-*b*-pGlu(O*t*Bu)$_{15}$) in CD_2Cl_2.

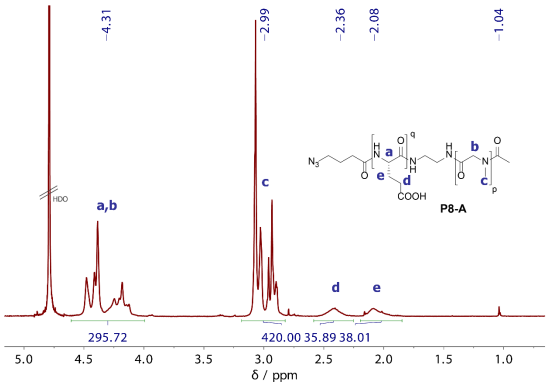

Figure S24. ^{1}H NMR spectrum of **P8-A** (pSar$_{140}$-*b*-pGlu(OH)$_{20}$) in D_2O.

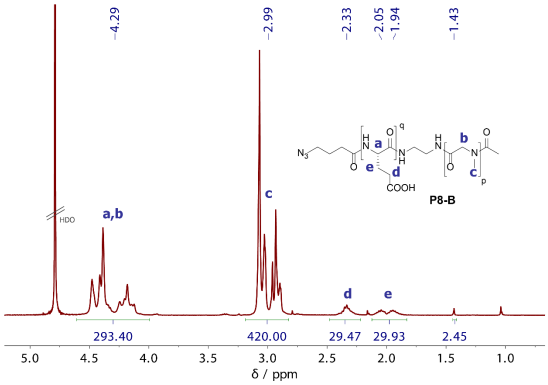

Figure S25. ^{1}H NMR spectrum of **P8-B** (pSar$_{140}$-*b*-pGlu(OH)$_{15}$) in D_2O.

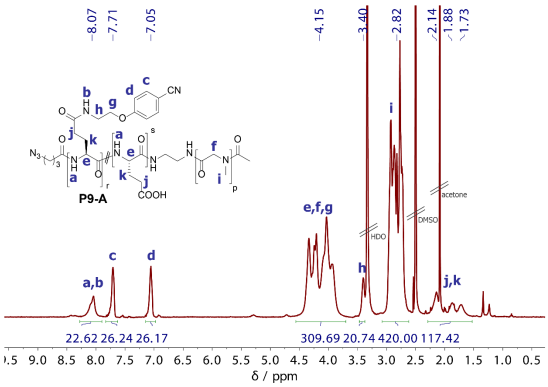

Figure S26. ^{1}H NMR spectrum of **P9-A** (pSar$_{140}$-*b*-pGlu(Mod)$_{20}$) in DMSO-*d*$_6$.

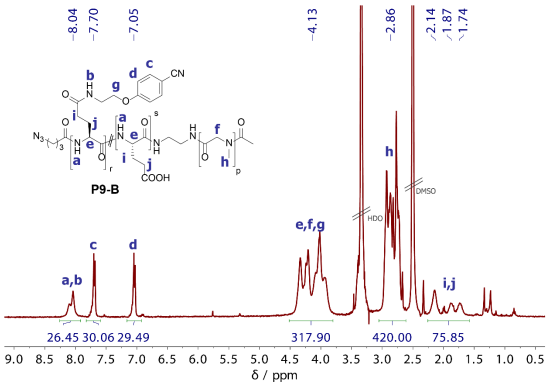

Figure S27. ^{1}H NMR spectrum of **P9-B** (pSar$_{140}$-*b*-pGlu(Mod)$_{15}$) in DMSO-*d*$_6$.

DOSY NMR Spectra

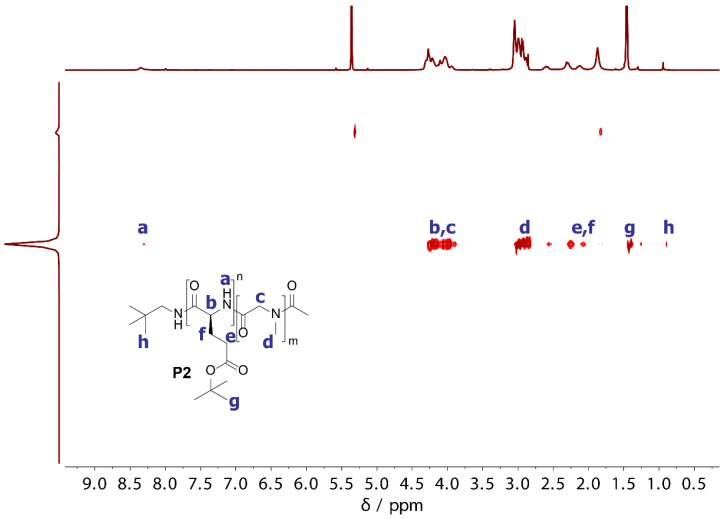

Figure S28. DOSY NMR spectrum of **P2** (pGlu(O*t*Bu)$_{36}$-*b*-pSar$_{171}$) in CD_2Cl_2.

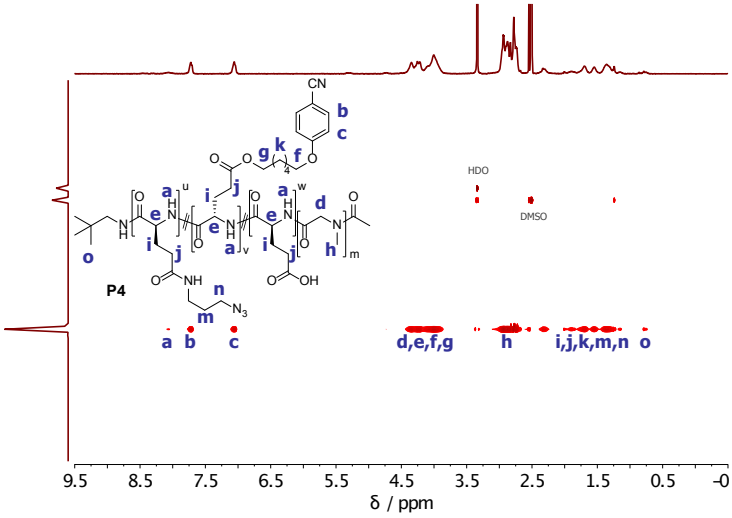

Figure S29. DOSY NMR spectrum of **P4** (pGlu(Mod)$_{36}$-*b*-pSar$_{171}$) in DMSO-d_6.

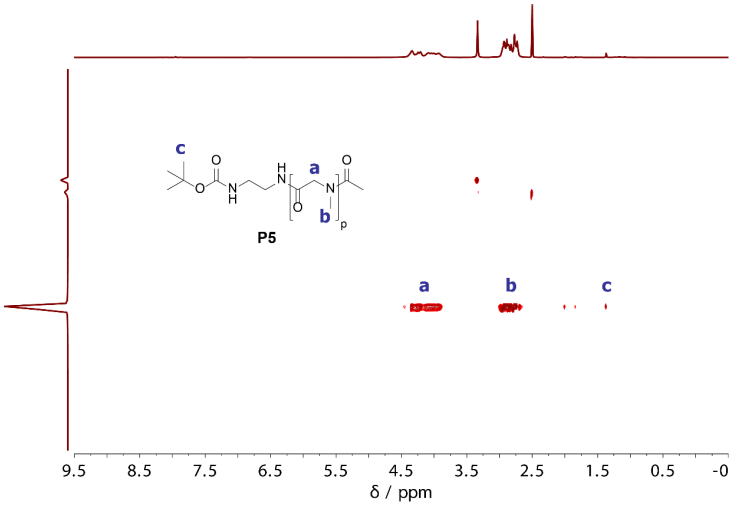

Figure S30. DOSY NMR spectrum of **P5** (*N*-Boc-pSar$_{140}$) in DMSO-d_6.

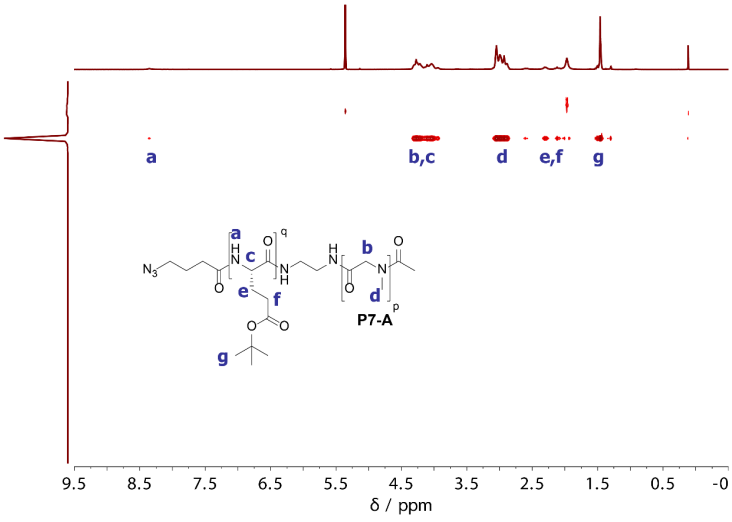

Figure S31. DOSY NMR spectrum of **P7-A** (pSar$_{140}$-*b*-pGlu(O*t*Bu)$_{20}$) in CD_2Cl_2.

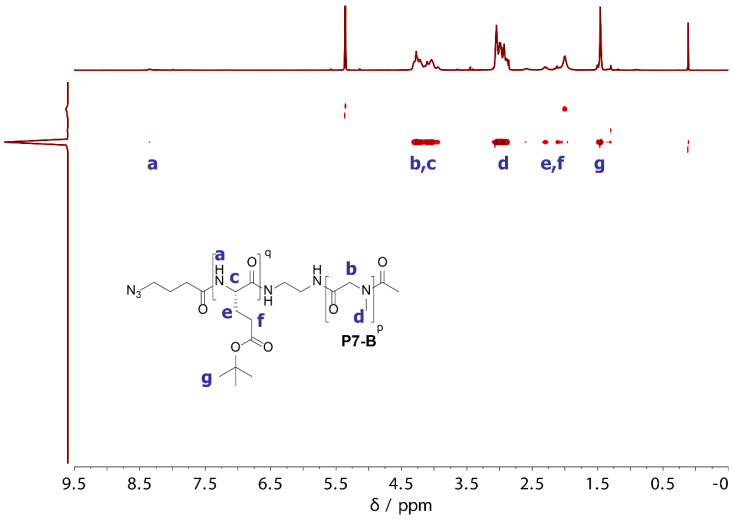

Figure S32. DOSY NMR spectrum of **P7-B** ($pSar_{140}$-*b*-$pGlu(OtBu)_{15}$) in CD_2Cl_2.

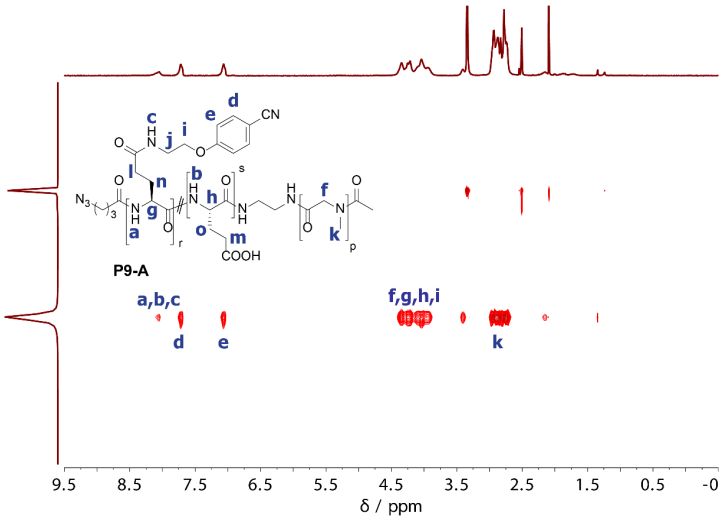

Figure S33. DOSY NMR spectrum of **P9-A** ($pSar_{140}$-*b*-$pGlu(Mod)_{20}$) in DMSO-d_6.